Atomic structure and physical properties of peridotite glasses at 1 bar

Charles Le Losq[1,2]* and Paolo A. Sossi[3]

[1]Université Paris Cité, Institut de Physique du Globe de Paris, CNRS, F-75005 Paris, France, [2]Research School of Earth Sciences, Australian National University, Canberra, ACT, Australia, [3]Institute of Geochemistry and Petrology, ETH Zürich, Zürich, Switzerland

Earth's mantle, whose bulk composition is broadly peridotitic, likely experienced periods of extensive melting in its early history that formed magma oceans and led to its differentiation and formation of an atmosphere. However, the physical behaviour of magma oceans is poorly understood, as the high liquidus temperatures and rapid quench rates required to preserve peridotite liquids as glasses have so far limited their investigation. In order to better characterize the atomic structure and estimate the physical properties of such glasses, we examined the Raman spectra of quenched peridotite melts, equilibrated at $1900°C \pm 50°C$ at ambient pressure under different oxygen fugacities (fO_2), from 1.9 log units below to 6.0 log units above the Iron-Wüstite buffer. Fitting the spectra with Gaussian components assigned to different molecular entities (Q-species) permits extraction of the mean state of polymerisation of the glass. We find that the proportions of Q^1 (0.36−0.32), Q^2 (0.50−0.43), and Q^3 (0.16−0.23) vary with Fe^{3+}/Fe^{TOT} ($Fe^{TOT} = Fe^{2+} + Fe^{3+}$), where increasing Fe^{3+}/Fe^{TOT} produces an increase in Q^3 at the expense of Q^2 at near-constant Q^1. To account for the offset between Raman-derived NBO/T (2.06−2.27) with those determined by assuming Fe^{2+} exists entirely as a network modifier and Fe^{3+} a network former (2.10−2.44), ~2/3 of the ferric iron and ~90% of the ferrous iron in peridotite glasses must behave as network modifiers. We employ a deep neural network model, trained to predict alkali and alkaline-earth aluminosilicate melts properties, to observe how small variations in the atomic structure of peridotite-like melts affect their viscosity. For Fe-free peridotite-like melts, the model yields a viscosity of ~ −1.75 log Pa s at 2000°C, similar to experimental determinations for iron-bearing peridotite melts. The model predicts that changes in the peridotite melt atomic structure with Fe^{3+}/Fe^{TOT} yield variations in melt viscosity lower than 0.1 log Pa s, barely affecting the Rayleigh number. Therefore, at the high temperatures typical of magma oceans, at least at 1 bar, small changes in melt structure from variations in oxidation state are unlikely to affect magma ocean fluid dynamics.

1 Introduction

Soon after their accretion or following giant impacts, several clues suggest the existence of extended magma oceans at the surface of terrestrial planets (Elkins-Tanton, 2012 and references therein). On Earth, the Earth-Theia Moon-forming collision would deposit sufficient energy to cause widespread melting (e.g., Tonks and Melosh, 1993; Abe, 1997; Canup, 2004; Canup, 2012). The convective dynamics of such a magma ocean would have

been critical for the formation and evolution of the Earth's early atmosphere, the segregation of its core and the crystallisation of its mantle (Schaefer and Fegley Jr, 2004; Labrosse et al., 2007; Rubie et al., 2007; Elkins-Tanton, 2012; Deguen et al., 2014; Canup et al., 2015; Landeau et al., 2016; Sossi et al., 2020). A key physical parameter of silicate liquids relevant to the dynamics of magma oceans is their viscosity, owing to its influence on the timescales over which convection, settling of crystals and metal-silicate emulsion occur (e.g., see reviews by Rubie et al., 2007; Elkins-Tanton, 2012). For instance, for a canonical Moon-forming impact, the impactor's core is expected to emulsify in the Earth's magma ocean post-collision (Karato and Murthy, 1997; Rubie et al., 2007). The viscosity of the magma ocean is thought to have been low enough (~0.1 Pa·s Liebske et al., 2005) to give rise to turbulent (hard) convection, characterized by a very high Rayleigh number, the non-dimensional ratio of thermal buoyancy forces to viscous and diffusive dissipative effects, in the 10^{28}–10^{30} range (Solomatov, 2007; Elkins-Tanton, 2012):

$$R_a = \frac{\rho g \alpha \Delta T L^3}{\eta \kappa}. \quad (1)$$

where ρ is the fluid density in $kg\,m^{-3}$, g is the gravitational acceleration in $m\,s^{-2}$, α is the thermal expansivity in K^{-1}, ΔT is the temperature range across the fluid that drives the convection in K, L is a characteristic length scale for the fluid body in m, η is dynamic viscosity in Pa·s, and κ is the thermal diffusivity in $m^2\,s^{-1}$. This should favour the emulsion of the impactor metal core, controlled by the ratio of the silicate melt viscosity $\eta_{silicate}$ and the metal viscosity η_{metal} (Wacheul et al., 2014):

$$r_\mu = \frac{\eta_{silicate}}{\eta_{metal}}. \quad (2)$$

The size of the metal droplets will depend on the equilibrium between inertial and surface tension forces; it is estimated to be in the centimeter range (Karato and Murthy, 1997; Wacheul et al., 2014).

Equations 1, 2 illustrate the importance of liquid viscosity in the various processes that shaped the evolution of a magma ocean(s) on the early Earth. To date, however, our understanding of melt viscosity for magma ocean-relevant melts is incomplete. For the Earth, assuming it was fully molten following a giant impact, likely had a magma ocean of peridotitic composition. However, there are few measurements of the viscosity of peridotite melt. Dingwell et al. (2004) determined the viscosity of komatiitic- to peridotitic melt (~32 wt% MgO) at 1 bar in air by concentric cylinder viscometry, finding log η ~ −0.95 Pa·s at 1860 K. They fit their data as a function of temperature to the Vogel–Fulcher–Tammann (VFT) equation;

$$log\,\eta = A + \frac{B}{T - C}, \quad (3)$$

where A = −4.31, B = 3703 and C = 761.7, and T the temperature in K. At higher pressures, up to 13 GPa, Liebske et al. (2005) determined the viscosity of peridotitic melts by the falling sphere method. They fit their data to a modified VFT equation to account for the effect of pressure, obtaining η between −1 and −2 log Pa·s up to 2500 K and 14 GPa. The recent measurements of Xie et al. (2021), which benefit from the latest advances in high speed camera (1,000 fps) determination of falling sphere velocities, indicate that

the effect of pressure on the viscosity of peridotite melt is limited at temperatures above 2000 K. In particular, along the liquidus, the viscosity decreases from 38 ± 2 mPa·s (log η = −1.42) at 2173 ± 100 K to 17 ± 1 mPa·s (log η = −1.77) at 2773 ± 150 K (Xie et al., 2021). These values are in line with falling sphere velocities determined by Cochain et al. (2017), applying *in situ* X-ray radiography of melts in the system $MSiO_3$ (where M = Ca or Mg), which show a modest decrease from ~200 mPa·s for $CaSiO_3$ and ~100 mPa·s for $MgSiO_3$ with increasing pressure from 1 bar up to ~7 GPa at temperatures near 2000 K. Viscosities of a variety of silicate melts, including peridotite and Fe_2SiO_4, converge to a common value near 20–30 mPa·s (log η = −1.6 ± 0.1) at 12–14 GPa (Spice et al., 2015; Cochain et al., 2017).

However, these measurements were performed under conditions that may not necessarily reflect those of a superficial magma ocean. For example, the experiments of Dingwell et al. (2004) were conducted without any control of fO₂, meaning the Fe^{3+}/Fe^{2+} ratios in their liquids were unconstrained. This is important as the Fe^{3+}/Fe^{2+} ratio in turn modifies melt viscosity, because ferric and ferrous iron occupy different structural roles in silicate melts (Dingwell et al., 1988; Dingwell and Virgo, 1988; 1989; Dingwell, 1991; Liebske et al., 2003; Chevrel et al., 2013). Indeed, in silicate melts, it is widely accepted that Fe^{3+} acts as a *network former*, participating more readily in the construction of the aluminosilicate polyhedral disordered network due to its preference for tetrahedral coordination, whereas Fe^{2+} acts as a *network modifier* that breaks T-O-T bonds (T = Si, Al), tending to occupy octahedral sites (see Le Losq et al., 2021b for a review). However, the coordination number (CN) of Fe^{2+} and Fe^{3+} varies as a function of composition, temperature, and pressure (e.g., Jackson et al., 2005; Zhang et al., 2017), implying that the relationship between melt structure, and, hence, viscosity with iron oxidation state, may not be straightforward. As a result, these variables need to be understood in order to ensure accurate prediction of silicate melt viscosities.

To evaluate how iron oxidation state could influence the rheology of silicate melts in magma oceans, we determine the atomic structure of peridotite glasses equilibrated at 1 bar and 1900 °C under different oxygen fugacities. The glasses were prepared by laser-heating aerodynamic levitation, under conditions representative of the surface of a terrestrial magma ocean (Sossi et al., 2020). Raman spectroscopy (Mysen et al., 1982; McMillan, 1984; McMillan et al., 1992; Neuville et al., 2014) was used to investigate the atomic structure of the glasses as a function of their Fe^{3+}/Fe^{TOT}. Such data permit better constraints to be placed on the role of iron and the atomic structure of peridotite melts at the surface of magma oceans, and, hence, inform models of the rheology of magma oceans and mineral-melt partition coefficients of elements like Fe and Mg.

2 Materials and methods

2.1 Glass synthesis

The glass samples were presented in the study of Sossi et al. (2020). The starting peridotite composition was synthesised by mixing and grinding a combination of oxide powders (>99.95% pure), MgO, SiO_2, Fe_2O_3, Al_2O_3, and $CaCO_3$ three times under ethanol in an agate mortar. The mixture was then decarbonated for 24 h in air at ~1,000 °C, and the resultant powder was pressed into pellets. Roughly 20-mg pieces of the

TABLE 1 Chemical composition in wt%, synthesis fO_2 and resulting Fe oxidation state, expressed as Fe^{3+}/Fe^{TOT} with Fe^{TOT} = $[Fe^{2+}]$ + $[Fe^{3+}]$, of the samples investigated in this study.

Sample	SiO_2	Al_2O_3	FeO(T)	MgO	CaO	$\log_{10} f(O_2)$	Fe^{3+}/Fe^{TOT}
Per-fO_2(1)	47.04 ± 0.21	4.34 ± 0.06	8.38 ± 0.17	37.61 ± 0.10	2.02 ± 0.02	0.00	0.440 ± 0.008
Per-fO_2(2)	46.69 ± 0.11	4.39 ± 0.03	8.53 ± 0.08	37.81 ± 0.15	2.07 ± 0.02	−2.49	0.277 ± 0.013
Per-fO_2(3)	46.61 ± 0.22	4.38 ± 0.05	8.63 ± 0.09	37.79 ± 0.12	2.07 ± 0.02	−2.53	0.269 ± 0.015
Per-fO_2(6)	46.72 ± 0.25	4.31 ± 0.05	8.58 ± 0.09	37.68 ± 0.13	2.07 ± 0.04	−2.72	0.226 ± 0.013
Per-TS1	46.45 ± 0.16	4.32 ± 0.05	8.87 ± 0.13	37.62 ± 0.10	2.04 ± 0.02	−2.72	0.267 ± 0.013
Per-fO_2(7)	46.75 ± 0.22	4.36 ± 0.04	8.71 ± 0.25	37.66 ± 0.10	2.07 ± 0.01	−2.72	0.240 ± 0.013
Per-TS2	46.50 ± 0.11	4.36 ± 0.05	8.56 ± 0.09	38.01 ± 0.18	2.08 ± 0.02	−2.72	0.217 ± 0.006
Per-fO_2(8)	46.06 ± 0.14	4.39 ± 0.04	8.66 ± 0.07	38.13 ± 0.13	2.08 ± 0.02	−3.00	0.172 ± 0.006
Per-fO_2(9)	46.11 ± 0.26	4.37 ± 0.05	8.21 ± 0.17	38.79 ± 0.06	1.96 ± 0.01	−3.92	0.124 ± 0.006
Per-fO_2(10)	46.71 ± 0.15	4.43 ± 0.04	8.47 ± 0.15	37.80 ± 0.30	2.11 ± 0.03	−5.32	0.045 ± 0.015
Per-fO_2(11)	46.22 ± 0.28	4.42 ± 0.04	7.89 ± 0.13	38.91 ± 0.18	2.12 ± 0.02	−6.74	0.019 ± 0.001
Per-fO_2(12)	46.53 ± 0.12	4.45 ± 0.08	7.80 ± 0.08	38.52 ± 0.16	2.15 ± 0.02	−7.86	0.014 ± 0.009

pellet were placed into the conical nozzle of the furnace, from which was fluxed a gas-mixture providing sufficient buoyancy to cause the molten silicate bead to levitate. Heating was achieved by a continuous wave 125-W CO_2 laser focused by gold-coated mirrors to a spot diameter of ~5 mm. All samples were melted once at 1900 °C ± 50 °C for 30 s in pure O_2 to achieve complete fusion and quenched to glass. Subsequently, the glass beads (diameters 1.45–2.05 mm) were equilibrated under different CO_2/H_2 gas mixtures diluted with 92% Ar, at temperatures of 1900 °C ± 50 °C, continuously recorded by an optical pyrometer. Quenching below the glass transition was achieved by switching off the laser, resulting in cooling rates of ~800 °C per second.

2.2 Glass characterisation

Glass compositions were measured by electron probe microanalysis (Sossi et al., 2020). On average, the composition, in wt%, is 46.5 ± 0.03 SiO_2, 4.37 ± 0.04 Al_2O_3, 8.4 ± 0.03 FeO, 38.0 ± 0.4 MgO, and 2.06 ± 0.05 CaO, with Na_2O and K_2O being both lower than 0.01. The oxidation state of the glasses was determined using Fe K-edge X-ray Absorption Near Edge Structure (XANES) spectroscopy at beamline 13IDE of the Advanced Photon Source, Argonne National Laboratories (IL, United States). All details are provided in Sossi et al. (2020). Table 1 provides the chemical composition and iron oxidation state of the samples investigated in this study.

2.3 Raman spectroscopy

In total, there are 12 different peridotite glasses with Fe^{3+}/Fe^{TOT} ranging from 0.01 to 0.44 (Sossi et al., 2020). Their Raman spectra were recorded using a Renishaw inVia spectrometer at the Australian National University. This Raman spectrometer is equipped with a Peltier-cooled detector, a 2400 lines/mm grating

and a confocal system. Samples were excited using a 532 nm laser line focused ~3 μm below the surface using a ×100 Leica objective; laser power on the sample was ~1.2 mW. The spatial resolution was <1 mm, and the spectral resolution ~1.2 cm^{-1}. Five spectra were recorded from different points for each sample. They were treated separately during the data reduction process. The combination of a laser power less than 5 mW (Di Genova et al., 2016) with a relatively short counting time of 120 s, and the analysis at five different points, was used to prevent Fe oxidation during spectral acquisition (Le Losq et al., 2019).

Pre-processing of the Raman spectra was done using the *Rampy* library in the Python programming language (Le Losq et al., 2019). The raw data were corrected from a linear background that was fit to the 1,180–1,300 cm^{-1} portions of the Raman spectra that are devoid of signal. Corrected spectra were normalized to the area under the curve.

To gather quantitative structural information from the Raman spectra, peak fitting was performed on the 700–1,300 cm^{-1} portion of the corrected Raman signals using the Bayesian approach described in Le Losq et al. (2022). In the Bayesian framework, the log *posterior* probability of a model is calculated from the sum of the log *likelihood* with the log *prior*. While the former describes how well a particular model fits the data, the latter embeds our initial knowledge about the problem, in the form of *a priori* probability distributions on model parameters. In this study, we used a single model composed of five peaks to fit all the spectra simultaneously. The choice of the number of peaks was made after observation of the spectra and consideration of results from previous studies on similar materials. The rationale for the number of peaks will be discussed in more detail in the Results section.

Gaussian, pseudo-Voigts and Lorentzian functions were tested to determine the most appropriate peak shapes to fit the data. The fits with the highest likelihoods are obtained using Gaussian peaks, in agreement with previous Raman studies of alkaline-earth alumino-silicate glasses (e.g., Mysen

TABLE 2 Prior values of the truncated normal distributions of amplitudes, frequencies and half width at half maximum (HWHM) of the peaks in the model.

Parameter	Mean	Standard deviation	Lower bond	Upper bond
R amplitudes	0.48	0.05	0	+inf
R frequencies	700.0	10.0	0	+inf
R HWHMs	50.0	5.0	0	+inf
Q^1 amplitudes	0.44	0.05	0	+inf
Q^1 frequency	873.0	5.0	850.0	910.0
Q^1 HWHM	39.0	5.0	20.0	+inf
Q^2 amplitudes	0.68	0.05	0	+inf
Q^2 frequency	940.0	5.0	910.0	1,000.0
Q^2 HWHM	56.0	5.0	40.0	+inf
Q^3 amplitudes	0.31	0.05	0	+inf
Q^3 frequency	1,021.0	5.0	1,000.0	+inf
Q^3 HWHM	64.0	5.0	40.0	+inf
$\theta^{Fe3+\text{-}O}$	0.2	0.03	0.05	0.5
Fe^{3+}-O frequency	923.0	5.0	900.0	970.0
Fe^{3+}-O HWHM	17.6	5.0	10.0	+inf

et al., 1982; Mysen et al., 1985a; Neuville, 2006). In the present model, we assume that Fe^{3+}/Fe^{TOT} has no influence on the frequencies and widths of the Gaussian peaks assigned to (Si,Al)-O stretching in Q^n units and Fe^{3+}-O stretching (see Results for details on attributions). Furthermore, while the intensities of the other peaks were considered as independent adjustable parameters, that of the peak assigned to Fe^{3+}-O stretching was calculated by multiplying the Fe^{3+}/Fe^{TOT} ratio by an adjustable parameter, $\theta^{Fe3+\text{-}O}$. This parameter can be considered as the equivalent of the Raman cross section of the signal assigned to Fe^{3+}-O. The log *likelihood* of the model is thus calculated using the 12 observed mean spectra of the 12 samples and those calculated using the model. The *prior* distributions of model parameters (intensities, positions, and widths) were set up using truncated Gaussian distributions, with means and standard deviations adjusted according to properties based on the decomposition of Raman spectra of depolymerised silicate glass compositions (e.g., from the studies of Mysen et al., 1982; Seifert et al., 1982; Neuville, 2006). Table 2 lists the *prior* mean and standard deviation values that were used.

The goal of the Bayesian approach adopted here is to obtain a sample of models, in which their statistical occurrence actually reflects their true probability distribution. Various methods allow obtaining this sample of models by sampling from the log posterior probability distribution. Here, we used the No-U-TurnS (NUTS) sampler (Hoffman and Gelman, 2014), implemented in the Python PyMC3 library (Salvatier et al., 2016), that relies on the Hamiltonian Monte Carlo (HMC) algorithm (Neal, 2012). The latter performs a random walk guided by Hamiltonian dynamics. After sampling one thousand models (initialization *advi-map*, 200,000 init steps, 2000 tuning steps), statistics on the different model

parameters were estimated. Convergence was checked *via* a visual inspection of the chains for each parameter, and *via* the Gelman-Rubin diagnostic criterion that was around one for each parameter. All subsequent calculations performed with model parameters (e.g., for calculating peak areas, Q^n unit fractions, etc.) were done using the full sample of models, such that reported results automatically take into account the propagation of errors. In this article, we report either the mean and σ values for parameters which distribution is approximately a normal one, or their median, and 2.5% and 97.5% quantiles in the other case.

3 Results

3.1 Glass Raman spectra

The Raman spectra of the glasses show two main large asymmetric bands located near 720 and 900–1,000 cm^{-1} (Figure 1). The first band can be assigned to a combination of inter-tetrahedral and rocking vibrations in the glass network (e.g., McMillan, 1984 and references therein). The second asymmetric band can be assigned to Si-O, Al-O and Fe^{3+}-O stretching in the polyhedral units building the glass aluminosilicate network. As the glass Fe^{3+}/Fe^{TOT} ratio increases, we observe an increase in the intensity of the ~720 cm^{-1} peak at the expense of the ~900 cm^{-1} band (Figure 1). In the 800–1,300 cm^{-1} portion of the Raman signals, the spectra of the reduced glasses define a clear maximum near 908 cm^{-1} and a shoulder near 950 cm^{-1}. With the oxidation of Fe, the intensity maximum shifts to ~930 cm^{-1} at Fe^{3+}/Fe^{TOT} = 0.44 and the signal intensity in the 1,000–1,150 cm^{-1} range increases.
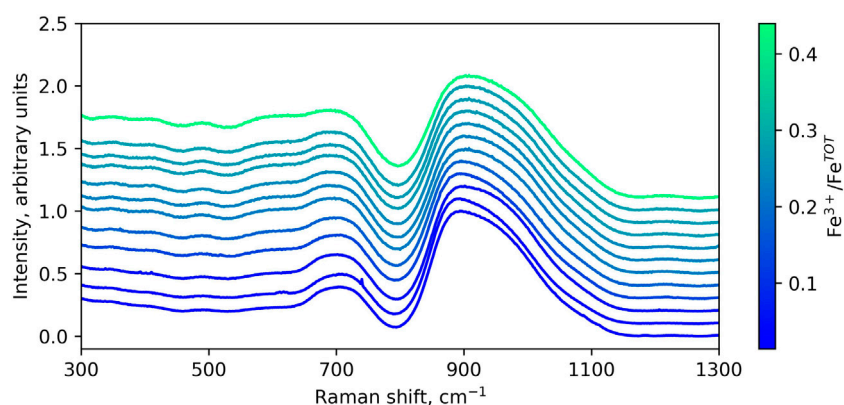
FIGURE 1
Raman spectra of the peridotite glasses. The color bar indicates the glass Fe^{3+}/Fe^{TOT}.

From the Raman spectra, quantitative information on the effect of the iron oxidation state on the glass structure can be gleaned by examining the $800–1,300 \text{ cm}^{-1}$ portion of the spectra, which contains the signals assigned to (Si,Al)-O stretching in the SiO_4-AlO_4 tetrahedral units that constitute the glasses. In the following, such structures are referred to as the Q^n tetrahedral units, with n their number of bridging oxygens (Schramm et al., 1984). Fully polymerized glasses like silica (pure SiO_2) are comprised exclusively of Q^4 units. In such a glass, Si^{4+} is a network former cation, as it participates in building a 3D tetrahedral network interconnected through bridging oxygens (BOs). Other potential network formers include Al^{3+} and Ti^{4+}. Adding monovalent or divalent metal cations $M^{+, 2+}$, such as Mg^{2+} or Na^+, to silica disrupts Si-O-Si bridges, and thus results in the formation of non-bridging oxygens (NBOs). As such, Q^n units with $n < 4$ characterise these depolymerized glasses, in proportions that depend on the bulk composition of the glass (e.g., Maekawa et al., 1991).

To quantify the degree of depolymerization, a useful parameter is the mean number of non-bridging oxygens per tetrahedral units, NBO/T, of the network. It ranges from 0 in fully polymerized glasses composed only of Q^4 units, to four in fully depolymerized glasses composed only of Q^0 units. Similarly, the NBO/T of Q^1 units is 3, that of Q^2 is 2, and that of Q^3 is 1. Regarding Fe^{2+} and Fe^{3+}, existing data generally indicate that the first acts as a *network modifier* cation, whereas the second acts as a *network former* cation (e.g., see the review in Le Losq et al., 2021b). Assuming such roles for Fe^{2+} and Fe^{3+}, the present glasses have an estimated NBO/T (calculated from composition as [2O-4T]/T with T the tetrahedral cations Si^{4+}, Al^{3+} and Fe^{3+}) that ranges from ~2.10 ($Fe^{3+}/Fe^{TOT} = 0.44$) to ~2.44 ($Fe^{3+}/Fe^{TOT} = 0.01$). Such an increase in NBO/T as Fe^{3+}/Fe^{TOT} decreases is in qualitative agreement with the decreasing intensity of the 700 cm^{-1} band that reflects a decrease in T-O-T bridging in the glass network.

Given the NBO/Ts of the present peridotite glasses, their atomic structure should mostly be composed of Q^2 units, with lower fractions of Q^1 and Q^3 units (e.g., see Maekawa et al., 1991). Considering that the peridotite glasses are also rich in MgO (38 wt%), a similar Q-species distribution to that of $MgSiO_3$ glass, with NBO/T = 2.00, might be expected. Enstatite glass
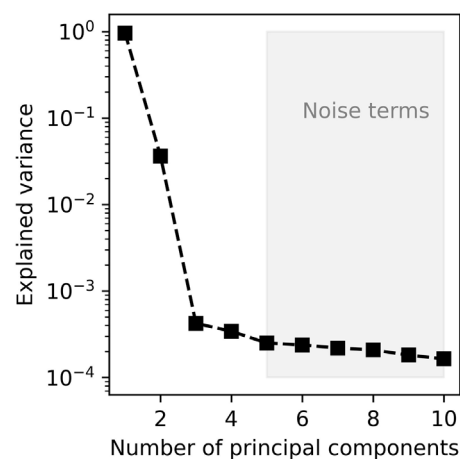

FIGURE 2
Principal component analysis of the $700−1,300 \text{ cm}^{-1}$ portion of the Raman spectra. Before the PCA analysis, preprocessing was done by removing the mean of the data.

comprises ~20–25% Q^1, ~39–42% Q^2, ~26–33% Q^3 and ~7–8% Q^4 (Sen et al., 2009; Spiekermann et al., 2013). This distribution is consistent with the shape of the $800–1,200 \text{ cm}^{-1}$ portion of the peridotite glass spectra, where three different features (such as peak maxima, shoulders, and slope breaks) visible near 900, 950 and $1,050 \text{ cm}^{-1}$ can be assigned to signals from T-O stretching in Q^1, Q^2 and Q^3 units, respectively (Brawer and White, 1975; Brawer and White, 1977; Virgo et al., 1980; Furukawa et al., 1981; Mysen et al., 1982; McMillan, 1984; Spiekermann et al., 2013). Furthermore, upon increasing Fe^{3+}/Fe^{TOT}, the intensity maximum near 900 cm^{-1} shifts to ~930 cm^{-1}, suggesting the presence of another vibrational mode near $920–930 \text{ cm}^{-1}$ that could be assigned to Fe^{3+}-O stretching (Virgo et al., 1982; Magnien et al., 2004; Roskosz et al., 2008; Di Muro et al., 2009; Di Genova et al., 2016; Le Losq et al., 2019), seeing as the bulk composition of the glass remains otherwise unchanged.
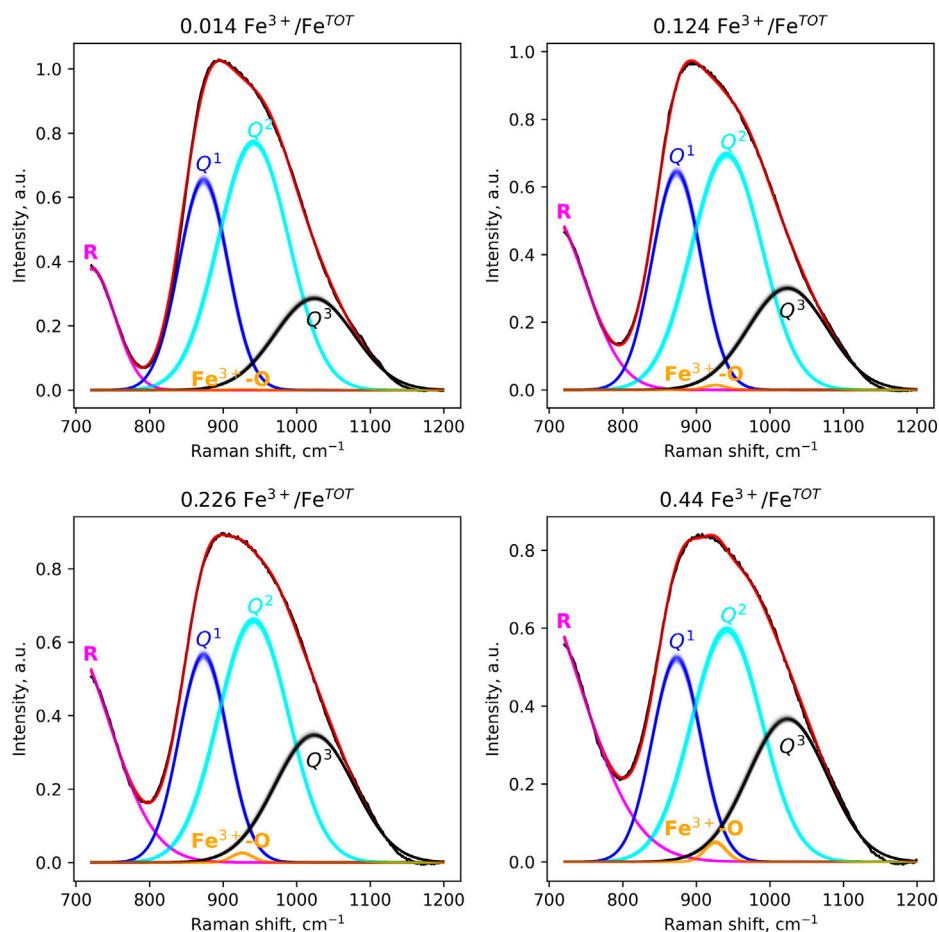
FIGURE 3
Peak-fitting models of the 800−1,200 cm^{-1} portion of Raman spectra of four peridotite glasses spanning the range of Fe^{3+}/Fe^{TOT} ratios. A subset of 200 posterior models, obtained by NUTS sampling (see Methods), are shown. The curves are affected by transparency coefficients, so that a more intense color means a higher density of models, and therefore a higher probability. All spectra are fit with a single model (see text). For one spectrum, the sum of its Gaussian components (pink, blue, cyan, black and orange lines) yields its fit (red line). The R band at ~720 cm^{-1} was used as a way to model properly the minimum in signal near 800 cm^{-1}.

3.2 Spectral model

Given the aforementioned considerations, the joint fit of the 700–1,200 cm^{-1} region of the spectra can be achieved with one peak near 700 cm^{-1}, hereafter named the R peak, to properly account for the background near 800 cm^{-1}, then four additional peaks in the 800–1,200 cm^{-1} range assigned to T-O (T = Si, Al) stretching in Q^1, Q^2 and Q^3 units as well as Fe^{3+}-O stretching in Fe^{3+}O$_4$ tetrahedral units. In order to assess the statistical number of Gaussian peaks required to fit the observed spectra, a principal component analysis (PCA) was undertaken (Figure 2). This exercise demonstrates that three to four components account for most of the variance in the 700–1,200 cm^{-1} region of the spectra (Figure 2), with additional components assigned to noise. Here, as independent constraints on the Fe^{3+}/Fe^{TOT} of the glasses are afforded *via* XANES (Sossi et al., 2020) we choose to decompose the spectra using a model with five discrete peaks, including one assigned to Fe^{3+}-O stretching that is constrained to covary with the Fe^{3+}/Fe^{TOT} of the glasses. In this manner, the degrees of freedom in the fits do not increase relative to

the number (3—4) required by the PCA analysis, and the variation in Fe^{3+}-O contribution is instructive to isolate the effect of this variable on the Raman spectra.

The model reproduces the Raman spectra of the samples to an excellent level of agreement (Figure 3). The addition of more peaks, which could be assigned to Q^0 or Q^4 units for instance, does not result in significant improvements in the fits (*cf.* Figure 2). The peak at ~873.4 cm^{-1} is assigned to T-O stretching in Q^1 units, that at ~941.6 cm^{-1} to T-O stretching in Q^2 units, and that at ~1,023.9 cm^{-1} to Q^3 units (Brawer and White, 1975; Brawer and White, 1977; Virgo et al., 1980; Furukawa et al., 1981; Mysen et al., 1982; McMillan, 1984; Mysen et al., 1985a; Spiekermann et al., 2013). The peak at ~926.0 cm^{-1} is assigned to Fe^{3+}-O stretching in Fe^{3+}O$_4$ tetrahedral units (Mysen et al., 1980; Virgo et al., 1982; Mysen et al., 1985a; 1985b; Cochain et al., 2012). The positions and widths of the peaks are provided in Table 3.

The intensities of the peaks vary with the glass Fe^{3+}/Fe^{TOT} in a continuous manner (Figure 4A). As Fe^{3+}/Fe^{TOT} increases, the intensities of the Q^1 and Q^2 peaks decrease, whereas those of the

TABLE 3 Median, 2.5 and 97.5 quantiles of the parameters of the Gaussian peaks used to model the spectra (see also Figure 2). As the R band was only used as a way to model properly background, no parameters are reported for this band.

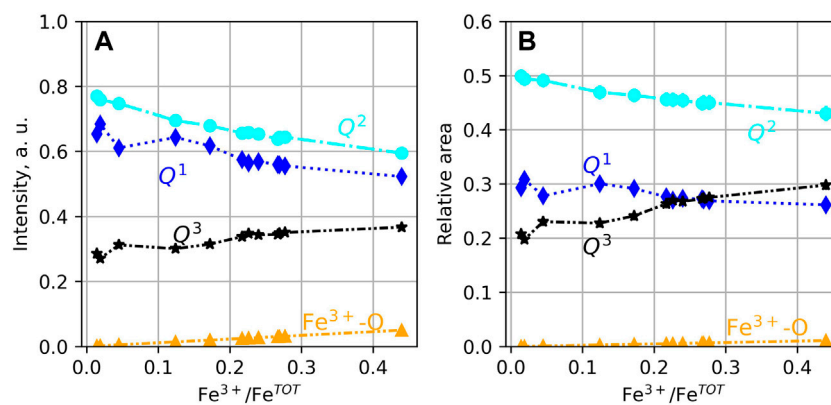| Peak	Raman shift, cm^{-1}	Half-width at half maximum (HWHM), cm^{-1}
Q^1	$873.4^{+0.3}_{-0.4}$	$39.1^{+0.2}_{-0.3}$
Q^2	$941.5^{+0.9}_{-1.0}$	$56.4^{+0.6}_{-0.8}$
Q^3	$1023.7^{+1.4}_{-1.7}$	$63.4^{+0.7}_{-0.6}$
$Fe^{3+}O_4$	$926.0^{+1.0}_{-1.0}$	$17.1^{+0.9}_{-0.9}$

FIGURE 4
(A) Intensity and **(B)** areas of the peaks assigned to (Si,Al)-O and Fe^{3+}-O stretching. If not visible, error bars are smaller than symbol size.

Q^3 and $Fe^{3+}O_4^{5-}$ peaks increase. The calculated areas of the peaks vary similarly (Figure 4B). We note that the area of the $Fe^{3+}O_4^{5-}$ peak is very small, nearly negligible compared to that of the other Q^n units. In general, the observations from Figure 4 indicate that increasing Fe^{3+}/Fe^{TOT} leads to increasing the fractions of Q^3 units at the expense of those of Q^1 and Q^2 units.

Using conversion coefficients θ^n, it is possible to convert the areas $A(Q^n)$ of the Raman peaks assigned to the different Q^n units (Figure 4B) into species concentrations $[Q^n]$ (e.g., Mysen and Frantz, 1993):

$$[Q^n] = \theta^n A(Q^n). \tag{4}$$

The determination of θ^n values requires the knowledge of $[Q^n]$, generally obtained from ^{29}Si Nuclear Magnetic Resonance (NMR) spectroscopy data. Using such an approach, Mysen (2007) determined that θ^3 = 1.05 ± 0.04 in sodium aluminosilicate glasses, and θ^3 = 1.06 ± 0.04 in hydrous sodium silicate glasses. From the analysis of their glass series; Mysen (2007) also proposed two values for θ^2: 1.06 ± 0.07 and 0.84 ± 0.07 for sodium aluminosilicate and hydrous sodium silicate compositions, respectively. Finally, from the study of Raman spectra of depolymerised hydrous sodium silicate glasses; Mysen (2007) proposed θ^1 = 0.22 ± 0.06. From the study of lithium silicate glasses, Umesaki et al. (1993) found that θ^3, θ^2, θ^1 and θ^0 values were 1.04, 1.02, 1.15 and 0.90, respectively. Recently, Nesbitt et al. (2021) proposed θ^3 =
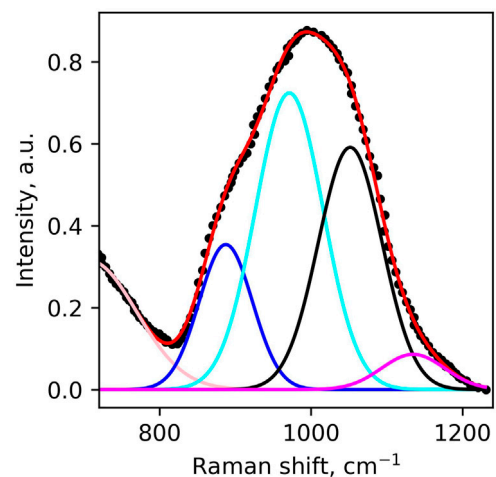

FIGURE 5
Peak fitting modeling of the Raman spectrum of enstatite glass. Original spectrum digitized from Kalampounias et al. (2009).

0.95 and θ^2 = 1.12 from the analysis of a sodium silicate glass with 40 mol% Na_2O.

To the best of our knowledge, there are no reported θ^n values for complex iron-bearing alkaline-earth alumino-silicate compositions. Furthermore, it is uncertain whether θ^n values
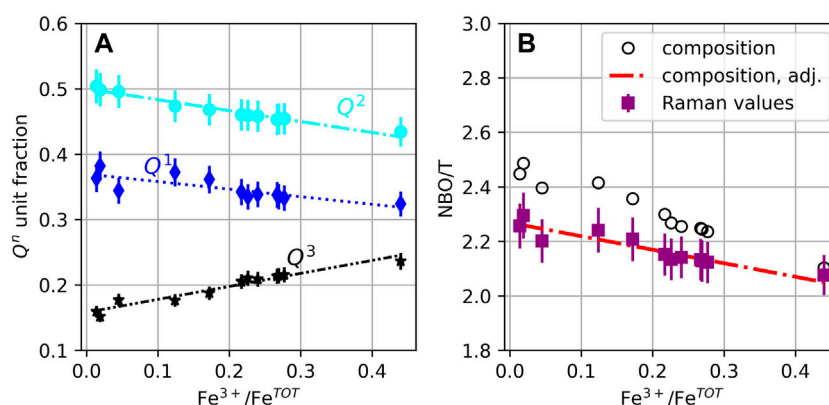
FIGURE 6
(A) Q^n unit fractions determined from the Raman data; lines are polynomial fits to the data. **(B)** Mean non-bridging oxygen atoms per tetrahedral units (NBO/T) calculated from the glass composition (black circles) and from the Raman-derived Q^n unit fractions in A (see Eq. 4, purple squares). The red dashed line marks the adjusted compositional trend, calculated assuming that ~66% of all Fe^{3+} cations act as network modifiers, and ~94% of all Fe^{2+} act as network modifiers (see discussion); the trend was corrected from a 0.15 absolute shift between stoichiometric and spectroscopic NBO/T values, observed for enstatite glass (Sen et al., 2009). If not visible, error bars are smaller than symbol size.

determined in alkali silicate- and aluminosilicate glasses are applicable to peridotite glasses. To test their applicability, we derive θ^n values from the fit of the Raman spectrum of enstatite $MgSiO_3$ glass. Indeed, its Mg-rich composition and NBO/T of two resemble those of the peridotite glasses, making it a suitable simplified analogue. Furthermore, the fractions of the different Q^n units in the enstatite glass have been determined precisely from 1D and 2D ^{29}Si Nuclear Magnetic Resonance (NMR) spectroscopy (Sen et al., 2009). Peak fitting the Raman spectrum of enstatite glass in the same manner as that of the peridotite glasses allows the quantification of the contributions from Q^1 to Q^4 units (Figure 5). The θ^n values are then simply obtained from the ratio between the true fraction of the Q^n unit and their normalized Raman peak areas. Using this approach, we determine $\theta^1 = 1.24 \pm 0.07$, $\theta^2 = 1.02 \pm 0.06$, $\theta^3 = 0.77 \pm 0.04$ and $\theta^4 = 1.42 \pm 0.09$.

Using the enstatite-derived θ^n values and Eq. 4, we convert the relative areas of the Raman peaks to fractions of Q^n units. The result is shown in Figure 6A. As Fe^{3+}/Fe^{TOT} increases from 0.01 to 0.44, the fraction of Q^1 units decreases from ~0.36 to ~0.32, that of Q^2 units decreases from ~0.50 to ~0.43, and that of Q^3 increases from ~0.16 to ~0.23. The subsequent NBO/T is given by

$$\text{NBO/T} = 3\left[Q^1\right] + 2\left[Q^2\right] + 1\left[Q^3\right]. \qquad (5)$$

Neglecting the influence of the $Fe^{3+}O_4$ peak as its contribution is very small and does not significantly affect the calculation of the NBO/T (Figures 2, 3), the NBO/T value decreases from ~2.26 to ~2.07 as Fe^{3+}/Fe^{TOT} increases from 0.01 to 0.44. These values can be compared with the NBO/T calculated from melt composition, assuming that Fe^{2+} acts only as a network modifier, and that Fe^{3+} acts only as a network former. The comparison shows that the compositionally determined NBO/T of reduced glasses are higher by ~0.2 compared to the Raman-determined values (Figure 6B). Furthermore, the slope $d(\text{NBO/T})/d(Fe^{3+}/Fe^{TOT})$ is steeper (i.e., a larger change in NBO/T for a given change in Fe^{3+}/Fe^{TOT}) than that of Raman-derived values.

4 Discussion

4.1 Raman modeling

The above analysis relies on the validity of the modeling of the broad signal assigned to Si-O and Al-O stretching in the 800–1,300 cm^{-1} portion of the spectra. In this study, we chose to follow the conventional approach that relies on using a limited number of symmetric peaks to decompose the observed signals (e.g., following the milestone study of Mysen et al., 1982). Each peak is assigned to T-O stretching in specific Q^n units and to Fe^{3+}-O stretching.

In detail, we consider this model a simplification of reality. Indeed, the true peak shapes of the T-O stretching signals assigned to Q^2, Q^3 and Q^4 units are not purely symmetric, as documented by studies of the Raman signals of silicate glasses relying on linear spectral decomposition (e.g., Zotov et al., 1999; Zakaznova-Herzog et al., 2007; Malfait, 2009; Herzog and Zakaznova-Herzog, 2011), atomistic simulations (Spiekermann et al., 2013), and peak fitting involving multiple symmetric peaks per Q^n units (e.g., see You et al., 2005; Osipov et al., 2015; Nesbitt et al., 2019; Nesbitt et al., 2021). The study of Spiekermann et al. (2013) presents simulation results on enstatite glass, and is thus particularly pertinent for our purposes. Their simulations reveal that the shape of the tetrahedral symmetric stretching signals (υ_1^{TET}) is, in general, asymmetric in the vibrational density of state of enstatite glass, particularly for Q^2 units. Therefore, the use of symmetric peaks in our peak-fitting model clearly is an approximation, but it was necessary because we could not determine the true shape of T-O stretching signals from Q^2, Q^3 and Q^4 units in the present peridotite glasses.

In the model, we also neglect the contributions of the asymmetric stretching of bridging oxygens in Q^n units, also referred to as υ_3^{BO} in Spiekerman et al. (2013), T_{2s} in Le Losq et al. (2022), or BO in Mysen et al. (1982). This simplification was made because the attempts at modeling the enstatite and peridotite spectra with an additional υ_3^{BO} peak were not successful. This may

be explained by the fact that $\upsilon_3{}^{BO}$ occurs at a frequency of ~950–1,050 cm^{-1} (Spiekermann et al., 2013) and thus strongly overlaps with the T-O stretching signals from Q^2 and Q^3 units in the spectra (Figures 3, 5). While it is usually possible to extract this signal from Raman spectra of relatively polymerized glasses (e.g., see Le Losq et al., 2022), here the signals in the 800–1,300 cm^{-1} portion of the Raman spectra of peridotite and enstatite glasses are broad and featureless. Because of this, attempts at introducing a new $\upsilon_3{}^{BO}$/T_{2s} band resulted in model instability and convergence failure. It was not possible to add a new $\upsilon_3{}^{BO}$/T_{2s} band without imposing strong constraints, and, hence, new sources of possible errors. Iron-bearing peridotite glasses present an even greater challenge, as the small Fe^{3+}-O signal overlaps part of the $\upsilon_1{}^{TET}$ Q^2 signal (Figure 3). The omission of the $\upsilon_3{}^{BO}$/T_{2s} peak may result in a systematic bias in the Q^1, Q^2, Q^3 and Q^4 peak areas, and hence in the θ^n values used for conversion of peak areas in $[Q^n]$ (Eq. 4). Therefore, given that we use the same model to fit the Raman spectra of both enstatite and peridotite glasses, the omission of the $\upsilon_3{}^{BO}$/T_{2s} peak results in no systematic change in Q^n species as any area offset is subsumed by the calibration of the θ^n values. Furthermore, several studies of depolymerized silicate glasses reveal near-negligible contributions of $\upsilon_3{}^{BO}$/T_{2s} signals in their Raman spectra (e.g., see Nesbitt et al., 2019; Nesbitt et al., 2021).

Despite the simplicity of the model employed herein, it produces excellent fits of the Raman spectra of peridotite and enstatite glasses (Figures 3, 5) and returns coherent Q^n unit concentrations and NBO/T values (see *Results* section and Figure 6). For the peridotite glasses, the number of introduced components also is consistent with the results of PCA (Figure 2). Together, these results indicate a robust and representative decomposition of Raman spectra of peridotite and enstatite glasses.

4.2 Structural role of iron in peridotite glasses

The conventional wisdom on the role of Fe^{2+} and Fe^{3+} in the atomic structure of silicate melts states that the former acts as a network modifier cation, breaking T-O-T bonds and creating NBOs, while the latter acts as a network former cation, like Al^{3+}, and participates in constructing the polyhedral network of the melt (e.g., see Le Losq et al., 2021b for a review). This structural picture is broadly corroborated by variations in the viscosity of silicate melts upon changing the redox state of iron. That is, at a given temperature, melt viscosity decreases as Fe^{3+} is reduced to Fe^{2+} (Dingwell et al., 1988; Dingwell, 1989; Liebske et al., 2003; Chevrel et al., 2013; Le Losq et al., 2021b). However, this general picture still is subject to debate because the coordination numbers (CNs) of Fe^{3+} and Fe^{2+} may vary with melt composition, which can, in turn, induce variations in melt properties.

In particular, while Fe^{3+} in CN 4 will act as a network former, forming true coordination polyhedra in the sense of Pauling (strong covalency of Fe-O bonds), Fe^{3+} that exists partially in CN 5 or 6 may not. Such considerations are important because multiple experimental studies support a mean Fe^{3+} CN higher than four in reduced glasses (e.g., Mysen et al., 1985a; Hannoyer et al., 1992; Farges et al., 2004; 2005; Jayasuriya et al., 2004; Liu and Lange, 2006; Wilke et al., 2007; Alderman et al., 2017; Zhang et al., 2018; Le Losq

et al., 2020). For instance, XANES spectra collected by Wilke et al. (2004) showed that the average CN of Fe^{3+} in sodium silicate and basaltic glasses is closer to 4.5 or 4.6. This agrees with earlier findings of Mysen et al. (1985b), Mysen et al. (1985a) and Virgo and Mysen (1985), all of whom suggested that, in reduced glasses with Fe^{3+}/Fe^{TOT} < ~0.5–0.6, $Fe^{3+}O_4{}^{5-}$ units coexist with $Fe^{3+}\cdot O_6{}^{9-}$. Such a conclusion is also supported by the more recent Mossbäuer and XANES studies of Jayasuriya et al. (2004), Alderman et al. (2017) and Zhang et al. (2018). These authors argue that the low Mossbäuer quadrupole splitting and isomer shift values in reduced glasses suggest that Fe^{3+} exists in CN higher than 4.

Similarly, Fe^{2+} dos not solely occupy octahedral coordination but has an average CN around ~5 in many silicate glasses, as indicated by Fe K-edge XANES studies (e.g., Wilke et al., 2004; 2007; Jackson et al., 2005; Le Losq et al., 2020) and Mossbäuer studies (e.g., Mysen, 2006; Zhang et al., 2018). In their diffraction study, Drewitt et al. (2013) confirm this assignment, showing that in ferrosilite, hedenbergite and fayalite liquids, Fe^{2+} is present in both CN 4 and CN 6, in proportions of roughly 50% $FeO_4{}^{6-}$ and 50% $FeO_6{}^{10-}$, with negligible $FeO_5{}^{8-}$. Regardless of its CN, ferrous iron is generally considered as a network modifier because of its low valence and its well-characterised effect on melt viscosity (e.g., Dingwell, 1991).

Here, information on the mean CNs of Fe^{2+} and Fe^{3+} was obtained from Fe K-edge X-Ray Absorption Near-Edge Structure (XANES) spectra of the peridotite glasses reported in Sossi et al. (2020). Indeed, relative to Raman spectroscopy, the Fe K-edge XANES region provides complementary information as to the structural and electronic environment of Fe in silicate glasses (e.g.; Berry et al., 2003; Wilke et al., 2004). In particular, the pre-edge feature that arises due to electronic transitions between bound- and excited states (in this case, the 1s → 3 d transition, Waychunas et al., 1983) can be used to estimate Fe^{3+}/Fe^{2+} and its mean coordination number. Bajt et al. (1994) demonstrated that the mean area-weighted centroid energies for Fe^{2+}- and Fe^{3+}-bearing compounds occur at ~7,112 eV and 7,113.5 eV, respectively, independent of their coordination environment. On the other hand, the pre-edge intensity of the ferrous- and ferric iron-related transitions depends on the coordination geometry of the site. In detail, centrosymmetric octahedral geometries result in low integrated intensities, whereas sites of low symmetry, such as tetrahedrally-coordinated Fe, produce higher intensity transitions for a given valence state of Fe (Wilke et al., 2001; Berry et al., 2003). One method used to calibrate the effect of oxidation state and coordination number on the pre-edge is predicated on the XANES measurement of minerals (Wilke et al., 2001; Wilke et al., 2004) to produce a variogram (Figure 7). Combinations of two discrete coordination geometries of different Fe valence states result in curvilinear mixing lines weighted towards the larger relative intensity contribution of the low symmetry site to the mean centroid energy. The use of the variogram to derive absolute oxidation states and coordination environments for glasses is subject to the caveat that, unlike minerals, glasses do not preserve long-range order. Therefore, we consider it as a guide, rather than as an absolute measure of bonding environment in glasses. This point is illustrated by the Anorthite-Diopside eutectic (ADeu) glass sample of Berry et al. (2003) synthesised at $\log fO_2$ = +4.8 at 1,409 °C, which plots outside the calibration range defined by the mineral end members (Figure 7).
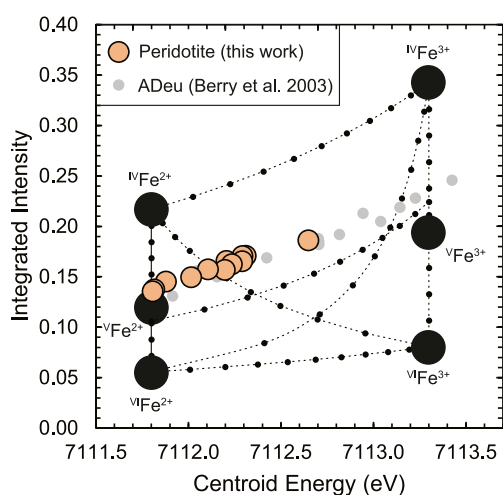
FIGURE 7
A variogram (after Wilke et al., 2004) that defines boundaries of
iron valence state and coordination number as a function of the
normalised integrated intensity of the XANES Fe K-edge pre-edge (1s
→ 3 d) feature against its mean centroid energy. The centroid
energy of the variogram is shifted downwards by 0.2 eV to match the
energy calibration used for the XANES spectra of Sossi et al. (2020).
The end member compositions (large black points) are deduced
based on Fe bonding environments in minerals, with the dashed
curves representing mixing lines between them (at increments of 0.1,
small black points). Data for peridotite glasses (orange points, this
work) are shown together with literature data for glasses of Anorthite-
Diopside eutectic (ADeu) composition (Berry et al., 2003), shifted
downwards by 0.3 eV to match the centroid energy of the peridotite
glasses when both sets have $Fe^{3+}/(Fe^{2+} + Fe^{3+}) = 0$. Error bars on points
are smaller than the circles.

glasses synthesised at ~500 °C lower temperatures and with a
considerably MgO-depleted, CaO-enriched composition with
respect to peridotite. This result suggests the structural and
electronic environment of Fe exhibits no resolvable, systematic
differences as a function of composition or temperature of
synthesis among ADeu and peridotitic glasses. The other
prevailing trend, commonly observed in silicate glasses (Knipping
et al., 2015; Alderman et al., 2017), is the tendency for Fe^{2+} to exist in
higher mean coordination environments than Fe^{3+}. The variogram
(Figure 7) indicates a mean coordination number of ~5.1 for Fe^{2+},
compared with ~4.7 for Fe^{3+}.

As these CN do not correspond to a discrete coordination
environment, Fe^{2+} and Fe^{3+} must reside in a distribution of
environments in peridotite glasses. This observation is important
because the extent to which each valence state affects NBO/T relates
to the structural roles they assume in melts, whereas the
compositional method for calculating NBO/T is binary, applying
the same weighting coefficient to each element (e.g., see footnote two
in Mysen et al., 1985). That is, each element is assumed to contribute
equally to either network formation or destruction. In contrast, Fe^{3+}
is proposed to show amphoteric behaviour on chemical grounds; it
can act either as an acidic or basic oxide, depending on the basicity of
the melt (Ottonello et al., 2001; Moretti, 2005; Ottonello, 2005;
Moretti and Ottonello, 2022). Hence, it can react with both bridging
and non-bridging oxygens, thus leading to variations in its local
environment as reflected by a variable CN (Moretti and Ottonello,
2022 and references cited therein).

We observe that, upon increasing Fe^{3+}/Fe^{TOT}, the Raman-
derived NBO/T decreases to a lesser extent than expected, should
all Fe^{3+} cations play a network-forming role (Figure 6B). This
observation indicates that Fe^{3+} may behave in an amphoteric
manner in the peridotite glasses. That is, some of the Fe^{3+}
cations act as network formers, while others do not and can be
considered as network modifiers. We can formalise this behaviour
by, first, taking into account the reaction between the three kinds of
oxygen atoms present in the melt atomic network (Fincham and
Richardson, 1954):

Nevertheless, the value of the variogram lies in the capacity for
direct comparison with other silicate glasses. The XANES spectra of
the peridotite glasses were fit according to the method outlined in
Sossi et al. (2020) and results are shown in Table 4 and Figure 7. The
glasses overlap, within uncertainty, with the trend defined by ADeu

TABLE 4 Mean centroid energy (eV) and normalised integrated intensity in peridotite glasses. See Sossi et al. (2020) for methods.

Sample	Mean centroid energy (eV)	Normalised integrated intensity	1σ
Per-fO_2 (1)	7,112.648	0.186	0.005
Per-fO_2 (2)	7,112.310	0.171	0.004
Per-fO_2 (3)	7,112.292	0.171	0.004
Per-fO_2 (6)	7,112.206	0.166	0.004
Per-TS1	7,112.291	0.165	0.004
Per-fO_2 (7)	7,112.235	0.163	0.004
Per-TS2	7,112.197	0.157	0.004
Per-fO_2 (8)	7,112.106	0.157	0.004
Per-fO_2 (9)	7,112.015	0.150	0.004
Per-fO_2 (10)	7,111.879	0.145	0.004
Per-fO_2 (11)	7,111.815	0.137	0.003
Per-fO_2 (12)	7,111.807	0.136	0.003

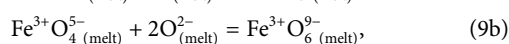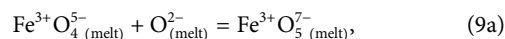$$2\,O^-_{(melt)} = O^{2-}_{(melt)} + O^0_{(melt)}, \tag{6}$$
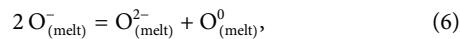
with O^- the NBOs, O^0 the BOs and O^{2-} the free (unbound) oxygens in the glass/melt. Upon glass synthesis, oxygen fugacity is imposed (Table 1) such that the equilibrium constant of the reaction (Moretti, 2005):

$$Fe^{2+}_{(melt)} + 1/4\,O_{2\,(gas)} = Fe^{3+}_{(melt)} + 1/2\,O^{2-}_{(melt)}, \tag{7}$$
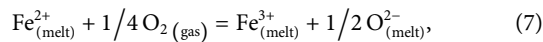
is defined. Reaction (7) accounts for the oxidation-reduction reaction between network modifiers Fe^{2+} and Fe^{3+}, but not for that involving Fe^{3+} in tetrahedral coordination (Ottonello et al., 2001; Moretti, 2005; Ottonello, 2005; Moretti and Ottonello, 2022). Another reaction is required to do so (Moretti and Ottonello, 2022):

$$Fe^{2+}_{(melt)} + 7/2\,O^{2-}_{(melt)} + 1/4\,O_{2\,(gas)} = Fe^{3+}O^{5-}_{4\,(melt)}, \tag{8}$$
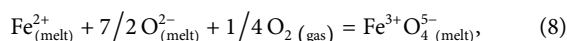
with $Fe^{3+}O_4^{5-}$ as a Fe^{3+} network former in tetrahedral coordination. It is the Fe^{3+}-O vibrations in such $Fe^{3+}O_4^{5-}$ units that yield the signal observed near 925 cm^{-1} in the Raman spectra (Figure 3). By the same token, a continued increase in aO^{2-} implies equilibria of the form

$$Fe^{3+}O^{5-}_{4\,(melt)} + O^{2-}_{(melt)} = Fe^{3+}O^{7-}_{5\,(melt)}, \tag{9a}$$

$$Fe^{3+}O^{5-}_{4\,(melt)} + 2O^{2-}_{(melt)} = Fe^{3+}O^{9-}_{6\,(melt)}, \tag{9b}$$

that control the distribution of IV-fold ($Fe^{3+}O_4^{5-}$), V-fold ($Fe^{3+}O_5^{7-}$) and VI-fold ($Fe^{3+}O_6^{9-}$) coordinated Fe^{3+} in the liquid. Hence, the oxidation of Fe^{2+} can produce both network forming (Eq. 8) and modifying (Eqs 9a, b) Fe^{3+}. The activity of free oxygens O^{2-}, driven by melt basicity and, hence, composition, will drive the equilibrium constants of reactions (7) to (9), and determine the different quantities of $Fe^{3+}O_4^{5-}$, $Fe^{3+}O_5^{7-}$ and $Fe^{3+}O_6^{9-}$ at given Fe^{3+}/Fe^{TOT} (Moretti and Ottonello, 2022). Upon oxidation, Eq. 8 will shift to the right-hand side, and be accompanied by network polymerisation (Figure 6A)

$$Q^1 + Q^2 = 2Q^3, \tag{10}$$

to an extent controlled by the equilibrium constants of reactions (9 a, b). The proposed amphoteric behaviour of Fe^{3+} in the alumino-silicate network of peridotite melts would explain the NBO/T *versus* Fe^{3+}/Fe^{TOT} trend derived from Raman data (Figure 6B), as well as the observed CN of Fe^{3+} (Figure 7). Indeed, as the formation of $Fe^{3+}O_4^{5-}$, $Fe^{3+}O_5^{7-}$ and $Fe^{3+}O_6^{9-}$ complexes occurs upon oxidation and with the increase in O^{2-} activity (Eqs 7–9), the fraction of NBO converted to BO must be lower than expected if assuming all Fe^{3+} were to play a network-forming role. As a consequence, the slope of the NBO/T versus Fe^{3+}/Fe^{TOT} trend based on the Raman spectra should be lower than predicted by the computationally derived NBO/T value. This prediction is borne out in Figure 6B, and suggests the coexistence of network former $Fe^{3+}O_4^{5-}$ with network modifier Fe^{3+} in CN 5 or 6 ($Fe^{3+}O_5^{7-}$ and $Fe^{3+}O_6^{9-}$ complexes in Eq. 9; Figure 7).

To quantify the proportions of Fe^{2+} and Fe^{3+} that act as network modifiers and formers, we reassign fractions of ferrous and ferric iron to tetrahedral T species $f_T^{Fe^{2+}}$ and $f_T^{Fe^{3+}}$, respectively), until the slope and intercept of the compositionally-derived calculation matches those of the Raman, using non-linear least-squares fitting. A systematic correction factor to the NBO/T of the Raman data of +0.15 is applied, given by the difference between the stoichiometric and NMR-derived NBO/T for enstatite glass (from the data of Sen et al., 2009). There are two simultaneous

equations, each with one unknown fraction $f_T^{Fe^{3+}}$ and $f_T^{Fe^{2+}}$, where $f_{modifier}^{Fe^{3+}} = 1 - f_T^{Fe^{3+}}$ and $f_{modifier}^{Fe^{2+}} = 1 - f_T^{Fe^{2+}}$. In order to fit the Raman NBO/T data (red line, Figure 6B) by solving for $f_T^{Fe^{3+}}$ and $f_T^{Fe^{2+}}$ indicates that, in the reduced, depolymerised peridotite glasses, most Fe^{2+} cations play a network modifier role (~94%), and, in fact, so too do most Fe^{3+} cations (~66% of total Fe^{3+}). Such values are consistent with the mean coordination number of Fe^{3+} given by XANES (~4.7; Figure 7). Indeed, if we assume that 34% of network former Fe^{3+} is in CN 4% and 66% of network modifier Fe^{3+} is in CN 5, then the mean CN of Fe^{3+} is expected to be ~4.7. Similarly, 6% of network former Fe^{2+} in CN 4 coexisting with ~78% CN 5 and ~16% CN 6 network-modifying Fe^{2+} yields the observed average CN of 5.1 (Figure 7). As noted above, the variogram should be used only as a guide, however, irrespective of the exact proportions of the coordination environments of Fe, the Raman and Fe K-edge XANES data point toward a significant fraction of Fe^{3+} acting as a network modifier in peridotite melts.

The equilibrium constants of reactions 7 to 9 should be strong functions of temperature and melt composition (Moretti, 2005; Moretti and Ottonello, 2022). In particular, with increasing temperature, we expect the equilibrium

$$2Q^2 = Q^1 + Q^3, \tag{11}$$

to shift to the right-hand side (e.g., Mysen and Frantz, 1993; Mysen, 1995; Mysen, 1996; Mysen, 1999). As temperature changes, this could influence the progress of reaction (10), such that we expect the ratio of $Fe^{3+}O_4^{5-}{}_{former}/Fe^{3+}{}_{modifier}$ to be temperature dependent. Comparison of aerodynamically levitated melts with their quenched counterparts show only marginal evidence for a temperature dependence of Eq. 9 (Alderman et al., 2017). However, XANES spectra of ultramafic compositions in the MgO-FeO-SiO$_2$ system are suggestive of an increase in CN in both Fe^{2+} and Fe^{3+} in melts with higher NBO/T, as expected from Eq. 9 and its ferrous iron equivalent.

High pressure conditions may also favour network modifier Fe^{3+}, as pressure tends to promote higher coordination environments for cations in silicate melts (e.g., Sanloup et al., 2013a; b; Wang et al., 2014; Drewitt et al., 2015; Sanloup, 2016) owing to their denser packing arrangements and therefore smaller molar volumes. In addition, pressure favours the conversion of Fe^{3+} to Fe^{2+} at given fO_2 (e.g., O'Neill et al., 2006; Zhang et al., 2017), at least up to ~9 GPa, above which the trend is reversed (Armstrong et al., 2019; Deng et al., 2020). Interestingly, the inflection point in Fe^{3+}/Fe^{2+} ratios observed in Armstrong et al. (2019) coincides with the viscosity decrease in the experiments of Liebske et al. (2005). Considering both effects, Fe in silicate melts at high pressures should be present at a significantly lower degree of polymerization (higher CN) relative to their low pressure counterparts. Indeed, ab-initio molecular dynamics (AIMD) simulations show evidence for higher mean Fe-O CN in peridotitic melts at 4000 K, from an average near ~4.5 at 1 bar to and reaching ~6 by 100 GPa (Huang et al., 2022). As a result, we speculate that, upon decompression, melt polymerization may occur as a result of pressure-induced oxidation of Fe^{2+} to Fe^{3+} and the subsequent transition of $Fe^{3+}{}_{modifier}$ to $Fe^{3+}O_4^{5-}{}_{former}$ as Fe^{3+} CN decreases, and that this melt polymerization should result in an increase in viscosity. Independent evidence for this comes from other AIMD simulations on basaltic melts, in which such liquids, at 2200 K, exhibit decreasing viscosities up to

~10 GPa before undergoing a drastic increase above these pressures (Bajgain et al., 2022). Such hypothesis is also in accord with the conclusions of Spice et al. (2015). Those authors observed that viscosity of molten fayalite at 1850°C increases by a factor of 2.5 when pressure decreases from 9.5 GPa to ambient. They reconciled their observations with the increase in <Fe-O> coordination with pressure observed by Sanloup et al. (2013a). Experimental investigation of glass or melt viscosities above 25 GPa would be key to reconciling structural changes with viscosity variations in deep magma oceans.

4.3 Evolution of the properties of peridotite melts in an early magma ocean

In an early magma ocean on Earth, the changing Fe redox state with temperature and fO_2 will yield variations in melt properties, including viscosity and density, that can affect the nature of convection. Previous viscosity measurements were performed at fixed or unconstrained fO_2 conditions, meaning these effects were not systematically investigated. The data at superliquidus temperatures on the $CaFeSi_2O_x$ composition indicate that its viscosity changes by less than 0.2 log Pa·s as Fe^{3+}/Fe^{TOT} increases from ~0.10 to ~0.85 (Dingwell, 1991). Taking this composition as an analogue for peridotite melts, only very limited variations in viscosity at superliquidus temperatures are expected, of the order of 0.1 log Pa·s as Fe^{3+}/Fe^{TOT} increases from 0.0 to 0.44.

Unfortunately, no general viscosity model, which could be used to predict the viscosity of peridotite melts, takes iron oxidation state into account. For instance, the Giordano et al. (2008) model, which uses polynomial interpolative functions to predict the effect of melt composition on viscosity, considers only the total iron concentration. The absence of a liquid viscosity model that includes the effect of Fe^{3+}/Fe^{TOT} is a consequence of the very few datasets that systematically examine how Fe^{3+}/Fe^{TOT} affects melt viscosity. In theory, this prevents an assessment of the effect of Fe^{3+}/Fe^{TOT} on melt viscosity in the context of this work. However, existing viscosity models and structural knowledge on the role of Fe^{2+} and Fe^{3+} in silicate and aluminosilicate glasses and melts can provide clues.

Indeed, as previously presented, a variety of spectroscopic methods attest to the prevailing role of Fe^{2+} as a network modifier cation in silicate melts, similar to Mg^{2+} or to Ca^{2+}, whereas Fe^{3+} behaves, at least partially, as a network former cation like Al^{3+} (see for a review of this Le Losq et al., 2021b,; Mysen and Richet, 2019). In general, this similarity arises from their similar ionic radii and charges, where Z/r for $^{IV}Al^{3+}$ = 7.7 and for $^{IV}Fe^{3+}$ = 6.1, while Z/r for $^{VI}Mg^{2+}$ = 2.78 and $^{VI}Fe^{2+}$ = 2.6 (Shannon et al., 1976). Therefore, we use Al^{3+} as an analogue for the network former $Fe^{3+}O_4^{5-}$, while the properties of either Mg^{2+} or Ca^{2+} are presumed to apply to network modifier Fe^{3+} and Fe^{2+}, such that Fe^{3+}/Fe^{TOT} variations are equivalent to variations in $Al^{3+}/(Al^{3+} + MO)$, with M = Ca or Mg. In this manner, the observed NBO/T variation as a function of Fe^{3+}/Fe^{TOT} is replicated: it varies from 2.45 for fully depolymerised reduced-like melts to 2.26 for oxydised-like melts (values here are uncorrected from the systematic shift between compositional and spectroscopic NBO/T, see Results section and Figure 6).

With these simplifications, the existing parametric model from Giordano et al. (2008) is employed to evaluate melt viscosity at 2000°C and 1 bar as a function of NBO/T. We further used an extension of the
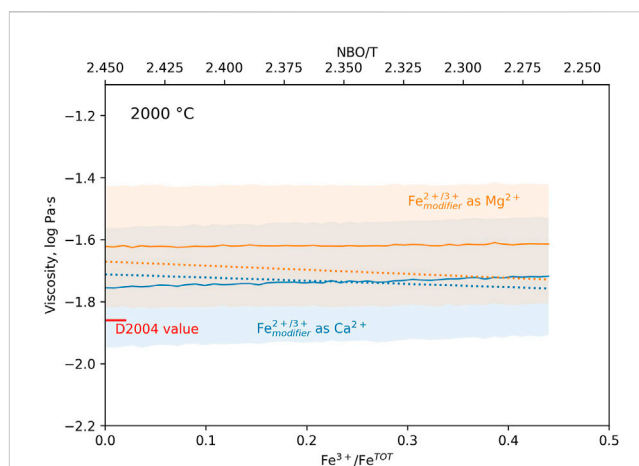

FIGURE 8
Viscosity (log Pa·s) of analogue peridotite melts at 2000 °C as a function of their Fe^{3+}/Fe^{TOT} and NBO/T. Here, network former $Fe^{3+}O_4^{5-}$ is assumed to behave analogous to Al^{3+} and network modifiers Fe^{3+} and Fe^{2+} as either Mg^{2+} (orange symbols and lines) or Ca^{2+} (blue symbols and lines). NBO/T varies from 2.45 for fully depolymerised reduced melts to 2.26 for oxidised-like melts (values uncorrected from the systematic shift between compositional and spectroscopic NBO/T). Solid lines are *i-Melt* predictions (see for model details Le Losq et al., 2021c), with errors indicated by the colored areas. Dotted lines are calculations performed with the Giordano et al. (2008) model. The red tick on the left annotated "D2004 value" refers to the viscosity value at 2000 °C determined from the extrapolation of the measurements of Dingwell et al. (2004) with the VFT equation.

i-Melt machine learning model (Le Losq et al., 2021c), trained to predict melt and glass properties (including viscosity) in the system $Na_2O-K_2O-CaO-MgO-Al_2O_3-SiO_2$ (Le Losq et al., 2021a). This version of *i-Melt* allows prediction of melt viscosity on the entire glass-forming domain of the $Na_2O-K_2O-CaO-MgO-Al_2O_3-SiO_2$ system with a mean test error of 0.4 log Pa·s.

At 2000°C, a temperature in the range of those inferred for magma oceans (e.g., Elkins-Tanton, 2012), calculated viscosities with both models range between −1.5 and −1.8 log Pa·s (Figure 8). The errors on the predictions from i-Melt were evaluated using MC Dropout (Gal and Ghahramani, 2016), and are lower than ± 0.3 log Pa·s (2σ) in the composition-temperature range of interest (Figure 8). In Figure 8, the NBO/T is recalculated from composition, taking into account that 66% of all Fe^{3+} cations and 94% of all Fe^{2+} cations act as network modifiers. At 2000°C, the measurements of Dingwell et al. (2004) are extrapolated to give a viscosity of −1.86 log Pa·s. We see thus a small shift between values from the *i-Melt* and Giordano et al. (2008) models presented in Figure 8 and the measurements of Dingwell et al. (2004). This is expected as the synthetic Fe-free peridotite-like melts are only an approximation of true peridotite melts, owing to the approximation that $Fe^{3+}O_4^{5-}$ behaves like $Al^{3+}O_4^{5-}$ in the melt structure, and modifiers Fe^{2+}/Fe^{3+} like Ca^{2+} or Mg^{2+}. It should also be noted that the composition of Dingwell et al. (2004) is poorer in MgO (~32 wt%) than our peridotite glasses (~38 wt%). Nevertheless, the models indicate that small variations in melt NBO/T induced by variations in the cationic ratio T^{3+}/M^{2+}, with T^{3+} a trivalent network former cation and M^{2+} a divalent network modifier cation, will generate limited viscosity variations at the very high, superliquidus

temperatures expected in magma oceans at their surface. Here, at most, we expect variations lower than 0.1 log Pa·s as the melt Fe^{3+}/Fe^{TOT} varies from 0.0 to 0.44 and its compositional NBO/T decreases by ~0.19 (Figure 8). This is within the previously highlighted range of expected variations when considering the experimental data of Dingwell (1991) on $CaFeSi_2O_x$ melts.

Such small variations in viscosity are unlikely to affect fluid dynamical processes. A simple calculation highlights this result. For instance we consider, a magma ocean of thickness = 1,000 km, composed of a silicate melt with constant $\rho = 3000 \, kg \, m^{-1}$ across its thickness, thermal diffusivity $\kappa = 10^{-8} \, m^2 \, s^{-1}$ (Eriksson et al., 2003) and thermal expansivity $\alpha = 10^{-4} \, K^{-1}$ (Gottsmann et al., 1999). The temperature gradient over its thickness is taken to be 1000 K. Of course, these values are only meant to be illustrative of those that could typify magma oceans and we neglect here the decrease in viscosity and changes in density with depth, given that our results are applicable only at 1 bar. Nevertheless, given $\eta_{silicate} = 10^{-1.86}$ Pa·s at 2000 °C, $R_a = 2.2 \times 10^{29}$. A small decrease of 0.1 in $\eta_{silicate}$ leads to $R_a = 1.8 \times 10^{29}$. Such variation is negligible, and such high R_a numbers simply indicate a very turbulent system in which viscous forces can be neglected. Naturally, from Eq. 1, only variations in $\eta_{silicate}$ of orders of magnitude can significantly influence R_a. In a magma ocean, such large variations in $\eta_{silicate}$ may originate from a large temperature gradient as well as extensive crystallization and degassing, which also can drive drastic changes in melt rheology (e.g., see Giordano et al., 2008; Mader et al., 2013 and references cited therein). It is therefore very unlikely that second-order parameters, such as small variations in melt composition and iron oxidation state, play a role in the dynamics of fluid flow in turbulent magma oceans, at least of peridotitic compositions at 1 bar. However, the effect of pressure also appears to be subordinate to that of temperature and crystallinity. Xie et al. (2021) report viscosities that are within uncertainty of one another between 10 and 25 GPa, though they are systematically a factor ~4 to 5 lower than that determined by Dingwell et al. (2004) at 1 bar. In other terms, and as expected, cooling and crystallization of magma oceans are likely the main factors leading to the death of turbulent, rapid fluid movements in such systems. Nevertheless, owing to diversity of compositions expected in rocky planets orbiting extrasolar systems from that of their host stars (e.g., Unterborn et al., 2020), the required order-of-magnitude variations in viscosity relative to peridotite could arise solely from changes in composition.

5 Conclusion

In this study, we analysed the Raman spectra of glasses with peridotitic composition synthesised at 2173 K and 1 bar, with Fe^{3+}/Fe^{TOT} ranging from 0.01 to 0.44. We find that the peridotite glasses are largely comprised of Q^2 units, with lower proportions of Q^1 and Q^3. The proportion of Q^3 units increases at the expense of those of Q^1 and Q^2 as Fe^{3+}/Fe^{TOT} increases. From these data, we calculate Raman-based NBO/T values as a function of Fe^{3+}/Fe^{TOT}. The change in NBO/T with Fe^{3+}/Fe^{2+} in the Raman-based methodology is less pronounced than that expected from compositional calculations that assume all Fe^{3+} cations play a network forming role. This suggests that Fe^{3+} cations act both as network formers and network modifiers in peridotitic silicate melts, confirming the amphoteric behavior of Fe^{3+} observed in aluminosilicate melts (Ottonello et al., 2001; Moretti, 2005;

Moretti and Ottonello, 2022). In fact, this behaviour is exaggerated in the present peridotite composition, as roughly two-thirds of the Fe^{3+} cations appear to act as network modifiers, while more than 90% of Fe^{2+} are network modifiers. As a result, changes in melt polymerisation as a function of Fe^{3+}/Fe^{2+} ratio are limited, with compositional NBO/T decreasing of ~0.19 as Fe^{3+}/Fe^{T} increases from ~0.01 to ~0.44. Using existing viscosity models and the machine learning model *i-Melt*, we show that such limited structural variations have an insignificant influence on melt viscosity, but are consistent with experimentally determined estimates of peridotite viscosity. We therefore conclude that any variations in the redox state of the Earth's magma ocean did not influence its convective vigour, although the variability of compositions among rocky exoplanetary mantles could be sufficiently different from that of peridotite to induce significant changes in Ra.

Data availability statement

The raw data supporting the conclusion of this article will be made available by the authors, without undue reservation.

Author contributions

CL and PS designed the idea during the 2021 CLEEDI workshop. Starting glass materials and XANES treatment were carried out by PS. CL analysed the glasses by Raman spectroscopy, interpreted the spectra, and produced the first draft of the manuscript. CL and PS contributed to the final manuscript.

Conflict of interest

The authors declare that the research was conducted in the absence of any commercial or financial relationships that could be construed as a potential conflict of interest.

Publisher's note

All claims expressed in this article are solely those of the authors and do not necessarily represent those of their affiliated organizations, or those of the publisher, the editors and the reviewers. Any product that may be evaluated in this article, or claim that may be made by its manufacturer, is not guaranteed or endorsed by the publisher.

References

Abe, Y. (1997). Thermal and chemical evolution of the terrestrial magma ocean. *Phys. Earth Planet. Interiors* 100, 27–39. doi:10.1016/s0031-9201(96)03229-3

Alderman, O. L. G., Wilding, M. C., Tamalonis, A., Sendelbach, S., Heald, S. M., Benmore, C. J., et al. (2017). Iron K-edge X-ray absorption near-edge structure spectroscopy of aerodynamically levitated silicate melts and glasses. *Chem. Geol.* 453, 169–185. doi:10.1016/j.chemgeo.2017.01.020

Armstrong, K., Frost, D. J., McCammon, C. A., Rubie, D. C., and Boffa Ballaran, T. (2019). Deep magma ocean formation set the oxidation state of Earth's mantle. *Science* 365, 903–906. doi:10.1126/science.aax8376

Bajgain, S. K., Ashley, A. W., Mookherjee, M., Ghosh, D. B., and Karki, B. B. (2022). Insights into magma ocean dynamics from the transport properties of basaltic melt. *Nature Comms.* 13 (1), 7590. doi:10.1038/s41467-022-35171-y

Bajt, S., Sutton, S. R., and Delaney, J. S. (1994). X-ray microprobe analysis of iron oxidation states in silicates and oxides using X-ray absorption near edge structure (XANES). *Geochimica Cosmochimica Acta* 58 (23), 5209–5214. doi:10.1016/0016-7037(94)90305-0

Berry, A. J., O'Neill, H. St. C., Jayasuriya, K. D., Campbell, S. J., and Foran, G. J. (2003). XANES calibrations for the oxidation state of iron in a silicate glass. *Am. Mineralogist* 88, 967–977. doi:10.2138/am-2003-0704

Brawer, S. A., and White, W. B. (1977). Raman spectroscopic investigation of the structure of silicate glasses (II). Soda-alkaline earth-alumina ternary and quaternary glasses. *J. Non-Crystalline Solids* 23, 261–278. doi:10.1016/0022-3093(77)90009-6

Brawer, S. A., and White, W. B. (1975). Raman spectroscopic investigation of the structure of silicate glasses. I. The binary alkali silicates. *J. Chem. Phys.* 63, 2421–2432. doi:10.1063/1.431671

Canup, R. M. (2004). Dynamics of lunar formation. *Annu. Rev. Astronomy Astrophysics* 42, 441–475. doi:10.1146/annurev.astro.41.082201.113457

Canup, R. M. (2012). Forming a Moon with an earth-like composition via a giant impact. *Science* 338, 1052–1055. doi:10.1126/science.1226073

Canup, R. M., Visscher, C., Salmon, J., and Jr, B. F. (2015). Lunar volatile depletion due to incomplete accretion within an impact-generated disk. *Nat. Geosci.* 8, 918–921. doi:10.1038/ngeo2574

Chevrel, M. O., Giordano, D., Potuzak, M., Courtial, P., and Dingwell, D. B. (2013). Physical properties of CaAl$_2$Si$_2$O$_8$–CaMgSi$_2$O$_6$–FeO–Fe$_2$O$_3$ melts: Analogues for extra-terrestrial basalt. *Chem. Geol.* 346, 93–105. doi:10.1016/j.chemgeo.2012.09.004

Cochain, B., Neuville, D. R., Henderson, G. S., McCammon, C. A., Pinet, O., and Richet, P. (2012). Effects of the iron content and redox state on the structure of sodium borosilicate glasses: A Raman, mössbauer and boron K-edge XANES spectroscopy study. *J. Am. Ceram. Soc.* 95, 962–971. doi:10.1111/j.1551-2916.2011.05020.x

Cochain, B., Sanloup, C., Leroy, C., and Kono, Y. (2017). Viscosity of mafic magmas at high pressures. *Geophys. Res. Lett.* 44, 818–826. doi:10.1002/2016GL071600

Deguen, R., Landeau, M., and Olson, P. (2014). Turbulent metal–silicate mixing, fragmentation, and equilibration in magma oceans. *Earth Planet. Sci. Lett.* 391, 274–287. doi:10.1016/j.epsl.2014.02.007

Deng, J., Du, Z., Karki, B. B., Ghosh, D. B., and Lee, K. K. M. (2020). A magma ocean origin to divergent redox evolutions of rocky planetary bodies and early atmospheres. *Nat. Commun.* 11, 2007. doi:10.1038/s41467-020-15757-0

Di Genova, D., Hess, K.-U., Chevrel, M. O., and Dingwell, D. B. (2016). Models for the estimation of Fe^{3+}/Fe^{tot} ratio in terrestrial and extraterrestrial alkali- and iron-rich silicate glasses using Raman spectroscopy. *Am. Mineralogist* 101, 943–952. doi:10.2138/am-2016-5534ccbyncnd

Di Muro, A., Métrich, N., Mercier, M., Giordano, D., Massare, D., and Montagnac, G. (2009). Micro-Raman determination of iron redox state in dry natural glasses: Application to peralkaline rhyolites and basalts. *Chem. Geol.* 259, 78–88. doi:10.1016/j.chemgeo.2008.08.013

Dingwell, D. B., Brearley, M., and Virgo, D. (1988). The dual role of ferric iron in liquid silicates: Effects on density & viscosity. *Chem. Geol.* 70, 86. doi:10.1016/0009-2541(88)90442-1

Dingwell, D. B., Courtial, P., Giordano, D., and Nichols, A. R. L. (2004). Viscosity of peridotite liquid. *Earth Planet. Sci. Lett.* 226, 127–138. doi:10.1016/j.epsl.2004.07.017

Dingwell, D. B. (1991). Redox viscometry of some Fe-bearing silicate melts. *Am. Mineralogist* 76, 1560–1562.

Dingwell, D. B. (1989). Shear viscosities of ferrosilicate liquids. *Am. Mineralogist* 74, 1038–1044.

Dingwell, D. B., and Virgo, D. (1988). Viscosities of melts in the Na$_2$O-FeO-Fe$_2$O$_3$-SiO$_2$ system and factors controlling relative viscosities of fully polymerized silicate melts. *Geochimica Cosmochimica Acta* 52, 395–403. doi:10.1016/0016-7037(88)90095-6

Dingwell, D. B., and Virgo, D. (1989). *Viscosity-oxidation state relationship for hedenbergitic melt.* United States: Carnegie Institution of Washington Year Book, 48–53. 87.

Drewitt, J. W. E., Jahn, S., Sanloup, C., de Grouchy, C., Garbarino, G., and Hennet, L. (2015). Development of chemical and topological structure in aluminosilicate liquids and glasses at high pressure. *J. Phys. Condens. Matter* 105103, 105103. doi:10.1088/0953-8984/27/10/105103

Drewitt, J. W. E., Sanloup, C., Bytchkov, A., Brassamin, S., and Hennet, L. (2013). Structure of (Fe$_x$Ca$_{1−x}$O)$_y$(SiO$_2$)$_{1−y}$ liquids and glasses from high-energy X-ray diffraction: Implications for the structure of natural basaltic magmas. *Phys. Rev. B* 87, 224201. doi:10.1103/PhysRevB.87.224201

Elkins-Tanton, L. T. (2012). Magma Oceans in the inner solar system. *Annu. Rev. Earth Planet. Sci.* 40, 113–139. doi:10.1146/annurev-earth-042711-105503

Eriksson, R., Hayashi, M., and Seetharaman, S. (2003). Thermal diffusivity measurements of liquid silicate melts. *Int. J. Thermophys.* 24, 785–797. doi:10.1023/a:1024048518617

Farges, F., Lefrère, Y., Rossano, S., Berthereau, A., Calas, G., and Brown, G. E., Jr. (2004). The effect of redox state on the local structural environment of iron in silicate glasses: A combined XAFS spectroscopy, molecular dynamics, and bond valence study. *J. Non-Crystalline Solids* 344, 176–188. doi:10.1016/j.jnoncrysol.2004.07.050

Farges, F., Rossano, S., Lefre, Y., Wilke, M., and Brown, G. E. B. (2005). Iron in silicate glasses a systematic analysis of PreEdge, XANES and EXAFS features. *Phys. Scr.* 957, 957. doi:10.1238/Physica.Topical.115a00957

Fincham, C. J. B., and Richardson, F. D. (1954). The behaviour of sulphur in silicate and aluminate melts. *Proc. R. Soc. Lond. A Math. Phys. Eng. Sci.* 223, 40–62. doi:10.1098/rspa.1954.0099

Furukawa, T., Fox, K. E., and White, W. B. (1981). Raman spectroscopic investigation of the structure of silicate glasses. III. Raman intensities and structural units in sodium silicate glasses. *J. Chem. Phys.* 75, 3226–3237. doi:10.1063/1.442472

Gal, Y., and Ghahramani, Z. (2016). Dropout as a bayesian approximation: Representing model uncertainty in deep learning international conference on machine learning (PMLR), 1050–1059. Available at: http://proceedings.mlr.press/v48/gal16.html (Accessed April 23, 2021).

Giordano, D., Russell, J. K., and Dingwell, D. B. (2008). Viscosity of magmatic liquids: A model. *Earth Planet. Sci. Lett.* 271, 123–134. doi:10.1016/j.epsl.2008.03.038

Gottsmann, J., Dingwell, D. B., and Gennaro, C. (1999). Thermal expansion of silicate liquids; direct determination using container-based dilatometry. *Am. Mineralogist* 84, 1176–1180. doi:10.2138/am-1999-7-821

Hannoyer, B., Lenglet, M., Dürr, J., and Cortes, R. (1992). Spectroscopic evidence of octahedral iron (III) in soda-lime silicate glasses. *J. Non-Crystalline Solids* 151, 209–216. doi:10.1016/0022-3093(92)90031-E

Herzog, F., and Zakaznova-Herzog, V. P. (2011). Quantitative Raman spectroscopy: Challenges, shortfalls, and solutions - application to calcium silicate glasses. *Am. Mineralogist* 96, 914–927. doi:10.2138/am.2011.3508

Hoffman, M. D., and Gelman, A. (2014). The No-U-turn sampler: Adaptively setting path lengths in Hamiltonian Monte Carlo. *J. Mach. Learn. Res.* 15, 1593–1623. doi:10.5555/2627435.2638586

Huang, D., Murakami, M., Brodholt, J., McCammon, C., and Petitgirard, S. (2022). Structural evolution in a pyrolitic magma ocean under mantle conditions. *Earth Planet. Sci. Lett.* 584, 117473. doi:10.1016/j.epsl.2022.117473

Jackson, W. E., Farges, F., Yeager, M., Mabrouk, P. A., Rossano, S., Waychunas, G. A., et al. (2005). Multi-spectroscopic study of Fe(II) in silicate glasses: Implications for the coordination environment of Fe(II) in silicate melts. *Geochimica Cosmochimica Acta* 69, 4315–4332. doi:10.1016/j.gca.2005.01.008

Jayasuriya, K. D., O'Neill, H. St. C., Berry, A. J., and Campbell, S. J. (2004). A Mössbauer study of the oxidation state of Fe in silicate melts. *Am. Mineralogist* 89, 1597–1609. doi:10.2138/am-2004-11-1203

Kalampounias, A. G., Nasikas, N. K., and Papatheodorou, G. N. (2009). Glass formation and structure in the MgSiO3–Mg2SiO4 pseudobinary system: From degraded networks to ioniclike glasses. *J. Chem. Phys.* 131, 114513. doi:10.1063/1.3225431

Karato, S., and Murthy, R. V. (1997). Core formation and chemical equilibrium in the Earth—I. Physical considerations. *Phys. Earth Planet. Interiors* 100, 61–79. doi:10.1016/S0031-9201(96)03232-3

Knipping, J. L., Behrens, H., Wilke, M., Göttlicher, J., and Stabile, P. (2015). Effect of oxygen fugacity on the coordination and oxidation state of iron in alkali bearing silicate melts. *Chem. Geol.* 411, 143–154. doi:10.1016/j.chemgeo.2015.07.004

Labrosse, S., Hernlund, J. W., and Coltice, N. (2007). A crystallizing dense magma ocean at the base of the Earth's mantle. *Nature* 450, 866–869. doi:10.1038/nature06355

Landeau, M., Olson, P., Deguen, R., and Hirsh, B. H. (2016). Core merging and stratification following giant impact. *Nat. Geosci.* 9, 786–789. doi:10.1038/ngeo2808

Le Losq, C., Baldoni, B., Valentine, A. P., and Neuville, D. R. (2021a). Modeling the properties of melts along calc-alkaline and alkaline magmatic differentiation trends using deep learning. in.

Le Losq, C., Berry, A. J., Kendrick, M. A., Neuville, D. R., and O'Neill, H. St. C. (2019). Determination of the oxidation state of iron in Mid-Ocean Ridge basalt glasses by Raman spectroscopy. *Am. Mineralogist* 104, 1032–1042. doi:10.2138/am-2019-6887

Le Losq, C., Cicconi, M. R., and Neuville, D. R. (2021b). "Iron in silicate glasses and melts," in *Magma redox geochemistry* (Washington, D.C.: American Geophysical Union), 233–253. doi:10.1002/9781119473206.ch12

Le Losq, C., Moretti, R., Oppenheimer, C., Baudelet, F., and Neuville, D. R. (2020). *In situ* XANES study of the influence of varying temperature and oxygen fugacity on iron oxidation state and coordination in a phonolitic melt. *Contrib. Mineral. Petrol* 175, 64. doi:10.1007/s00410-020-01701-4

Le Losq, C., Mysen, B. O., and Cody, G. D. (2022). Water solution mechanism in calcium aluminosilicate glasses and melts: Insights from *in* and *ex situ* Raman and ^{29}Si NMR spectroscopy. *Comptes Rendus Géoscience* 354, 199–225. doi:10.5802/crgeos.127

Le Losq, C., Valentine, A. P., Mysen, B. O., and Neuville, D. R. (2021c). Structure and properties of alkali aluminosilicate glasses and melts: Insights from deep learning. *Geochimica Cosmochimica Acta* 314, 27–54. doi:10.1016/j.gca.2021.08.023

Liebske, C., Behrens, H., Holtz, F., and Lange, R. A. (2003). The influence of pressure and composition on the viscosity of andesitic melts. *Geochimica Cosmochimica Acta* 67, 473–485. doi:10.1016/S0016-7037(02)01139-0

Liebske, C., Schmickler, B., Terasaki, H., Poe, B., Suzuki, A., Funakoshi, K., et al. (2005). Viscosity of peridotite liquid up to 13 GPa: Implications for magma ocean viscosities. *Earth Planet. Sci. Lett.* 240, 589–604. doi:10.1016/j.epsl.2005.10.004

Liu, Q., and Lange, R. A. (2006). The partial molar volume of Fe_2O_3 in alkali silicate melts: Evidence for an average Fe^{3+} coordination number near five. *Am. Mineralogist* 91 (2-3), 385–393. doi:10.2138/am.2006.1902

Mader, H. M., Llewellin, E. W., and Mueller, S. P. (2013). The rheology of two-phase magmas: A review and analysis. *J. Volcanol. Geotherm. Res.* 257, 135–158. doi:10.1016/j.jvolgeores.2013.02.014

Maekawa, H., Maekawa, T., Kawamura, K., and Yokokawa, T. (1991). The structural groups of alkali silicate glasses determined from ^{29}Si MAS-NMR. *J. Non-Crystalline Solids* 127, 53–64. doi:10.1016/0022-3093(91)90400-Z

Magnien, V., Neuville, D. R., Cormier, L., Mysen, B. O., Briois, V., Belin, S., et al. (2004). Kinetics of iron oxidation in silicate melts: A preliminary XANES study. *Chem. Geol.* 213, 253–263. doi:10.1016/j.chemgeo.2004.08.047

Malfait, W. J. (2009). Quantitative Raman spectroscopy: Speciation of cesium silicate glasses. *J. Raman Spectrosc.* 40, 1895–1901. doi:10.1002/jrs.2338

McMillan, P. F. (1984). Structural studies of silicate glasses and melts - applications and limitations of Raman spectroscopy. *Am. Mineralogist* 69, 622–644.

McMillan, P. F., Wolf, G. H., and Poe, B. T. (1992). Vibrational spectroscopy of silicate liquids and glasses. *Chem. Geol.* 96, 351–366. doi:10.1016/0009-2541(92)90064-c

Moretti, R., and Ottonello, G. (2022). "Silicate melt thermochemistry and the redox state of magmas," in Geological melts *reviews in mineralogy & geochemistry* (Chantilly: Mineralogical Society of America), 339–403.

Moretti, R. (2005). Polymerisation, basicity, oxidation state and their role in ionic modelling of silicate melts. *Ann. Geophys.* 48. doi:10.4401/ag-3221

Mysen, B. O. (1995). Experimental, *in situ*, high-temperature studies of properties and structure of silicate melts relevant to magmatic processes. *Eur. J. Mineralogy* 7, 745–766. doi:10.1127/ejm/7/4/0745

Mysen, B. O., Finger, L. W., Virgo, D., and Seifert, F. A. (1982). Curve-fitting of Raman spectra of silicate glasses. *Am. Mineralogist* 67, 686–695.

Mysen, B. O., and Frantz, J. D. (1993). Structure of silicate melts at high temperature: *In-situ* measurements in the system BaO-SiO$_2$. *Am. Mineralogist* 78, 699–709.

Mysen, B. O. (1996). Haploandesitic melts at magmatic temperatures: *In situ*, high-temperature structure and properties of melts along the join K$_2$Si$_4$O$_9$-K$_2$(KAl)$_4$O$_9$ to 1236 °C at atmospheric pressure. *Geochimica Cosmochimica Acta* 60, 3665–3685. doi:10.1016/0016-7037(96)00198-6

Mysen, B. O., and Richet, P. (2019). *Silicate glasses and melts*. 2nd ed. Amsterdam: Elsevier.

Mysen, B. O., Scarfe, C. M., and Cronin, D. J. (1985a). Viscosity and structure of iron- and aluminum-bearing calcium silicate melts at 1 atm. *Am. Mineralogist* 70, 487–498.

Mysen, B. O., Seifert, F., and Virgo, D. (1980). Structure and redox equilibria of iron-bearing silicate melts. *Am. Mineralogist* 65, 867–884.

Mysen, B. O. (1999). Structure and properties of magmatic liquids: From haplobasalt to haploandesite. *Geochimica Cosmochimica Acta* 63, 95–112. doi:10.1016/s0016-7037(98)00273-7

Mysen, B. O. (2007). The solution behavior of H$_2$O in peralkaline aluminosilicate melts with implications for properties of hydrous melts. *Geochimica Cosmochimica Acta* 71, 1820–1834. doi:10.1016/j.gca.2007.01.007

Mysen, B. O. (2006). The structural behavior of ferric and ferrous iron in aluminosilicate glass near meta-aluminosilicate joins. *Geochimica Cosmochimica Acta* 70, 2337–2353. doi:10.1016/j.gca.2006.01.026

Mysen, B. O., Virgo, D., Neumann, E.-R., and Seifert, F. A. (1985b). Redox equilibria and the structural states of ferric and ferrous iron in melts in the system CaO-MgO-Al$_2$O$_3$-SiO$_2$-Fe-O: Relationships between redox equilibria, melt structure and liquidus phase equilibria. *Am. Mineralogist* 70, 317–331.

Mysen, B. O., Virgo, D., and Seifert, F. A. (1985). Relationships between properties and structure of aluminosilicate melts. *Am. Mineralogist* 70, 88–105.

Neal, R. M. (2012). MCMC using Hamiltonian dynamics. arXiv:1206.1901 [physics, stat]. Available at: http://arxiv.org/abs/1206.1901 (Accessed July 24, 2018).

Nesbitt, H. W., Henderson, G. S., Bancroft, G. M., and Neuville, D. R. (2021). Spectral Resolution and Raman Q^3 and Q^2 cross sections in ~40 mol% Na$_2$O glasses. *Chem. Geol.* 562, 120040. doi:10.1016/j.chemgeo.2020.120040

Nesbitt, H. W., O'Shaughnessy, C., Henderson, G. S., Michael Bancroft, G., and Neuville, D. R. (2019). Factors affecting line shapes and intensities of Q^3 and Q^4 Raman bands of Cs silicate glasses. *Chem. Geol.* 505, 1–11. doi:10.1016/j.chemgeo.2018.12.009

Neuville, D. R., de Ligny, D., and Henderson, G. S. (2014). "Advances in Raman spectroscopy applied to earth and material sciences," in *Reviews in mineralogy and geochemistry* (Chantilly: Mineralogical Society of America), 509–541.

Neuville, D. R. (2006). Viscosity, structure and mixing in (Ca, Na) silicate melts. *Chem. Geol.* 229, 28–41. doi:10.1016/j.chemgeo.2006.01.008

O'Neill, H. St. C., Berry, A. J., McCammon, C. C., Jayasurika, K. D., Campbell, S. J., and Foran, G. (2006). An experimental determination of the effect of pressure on the Fe^{3+}/ΣFe ratio of an anhydrous silicate melt to 3.0 GPa. *Am. Mineralogist* 91, 404–412. doi:10.2138/am.2005.1929

Osipov, A., Osipova, L., and Zainullina, R. (2015). Raman spectroscopy and statistical analysis of the silicate species and group connectivity in cesium silicate glass forming system. *Int. J. Spectrosc.* 2015, 1–15. doi:10.1155/2015/572840

Ottonello, G. (2005). Chemical interactions and configurational disorder in silicate melts. Annals of Geophysics. Available at: http://www.earth-prints.org/handle/2122/924 (Accessed June 27, 2016).

Ottonello, G., Moretti, R., Marini, L., and Vetuschi Zuccolini, M. (2001). Oxidation state of iron in silicate glasses and melts: A thermochemical model. *Chem. Geol.* 174, 157–179. doi:10.1016/S0009-2541(00)00314-4

Roskosz, M., Toplis, M. J., Neuville, D. R., and Mysen, B. O. (2008). Amorphous materials: Properties, structure, and durability: Quantification of the kinetics of iron oxidation in silicate melts using Raman spectroscopy and assessment of the role of oxygen diffusion. *Am. Mineralogist* 93, 1749–1759. doi:10.2138/am.2008.2861

Rubie, D. C., Nimmo, F., and Melosh, H. J. (2007). "formation of Earth's core," in *Treatise on geophysics*. Editor G. Schubert (Amsterdam: Elsevier), 51–90. doi:10.1016/B978-044452748-6.00140-1

Salvatier, J., Wiecki, T. V., and Fonnesbeck, C. (2016). Probabilistic programming in Python using PyMC3. *PeerJ Comput. Sci.* 2, e55. doi:10.7717/peerj-cs.55

Sanloup, C. (2016). Density of magmas at depth. *Chem. Geol.* 429, 51–59. doi:10.1016/j.chemgeo.2016.03.002

Sanloup, C., Drewitt, J. W. E., Crépisson, C., Kono, Y., Park, C., McCammon, C., et al. (2013a). Structure and density of molten fayalite at high pressure. *Geochimica Cosmochimica Acta* 118, 118–128. doi:10.1016/j.gca.2013.05.012

Sanloup, C., Drewitt, J. W. E., Konôpková, Z., Dalladay-Simpson, P., Morton, D. M., Rai, N., et al. (2013b). Structural change in molten basalt at deep mantle conditions. *Nature* 503, 104–107. doi:10.1038/nature12668

Schaefer, L., and Fegley, B., Jr. (2004). A thermodynamic model of high temperature lava vaporization on Io. *Icarus* 169, 216–241. doi:10.1016/j.icarus.2003.08.023

Schramm, C. M., de Jong, B. H. W. S., and Parziale, V. E. (1984). Silicon-29 magic angle spinning NMR study on local silicon environments in amorphous and crystalline lithium silicates. *J. Am. Chem. Soc.* 106, 4396–4402. doi:10.1021/ja00328a018

Seifert, F., Mysen, B. O., and Virgo, D. (1982). Three-dimensional network structure of quenched melts (glass) in the systems SiO$_2$-NaAlO$_2$, SiO$_2$-CaAl$_2$O$_4$ and SiO$_2$-MgAl$_2$O$_4$. *Am. Mineralogist* 67, 696–717.

Sen, S., Maekawa, H., and Papatheodorou, G. N. (2009). Short-range structure of invert glasses along the pseudo-binary join MgSiO$_3$–Mg$_2$SiO$_4$: Results from 29Si and 25Mg MAS NMR spectroscopy. *J. Phys. Chem. B* 113, 15243–15248. doi:10.1021/jp9079603

Shannon, R. D. (1976). Revised effective ionic radii and systematic studies of interatomic distances in halides and chalcogenides. *Acta Crystallogr. Sect. A* 32, 751–767. doi:10.1107/S0567739476001551

Solomatov, V. (2007). "9.04 - magma Oceans and primordial mantle differentiation," in *Treatise on geophysics*. Editor G. Schubert (Amsterdam: Elsevier), 91–119. doi:10.1016/B978-044452748-6.00141-3

Sossi, P. A., Burnham, A. D., Badro, J., Lanzirotti, A., Newville, M., and O'Neill, H. St. C. (2020). Redox state of Earth's magma ocean and its Venus-like early atmosphere. *Sci. Adv.* 6, eabd1387. doi:10.1126/sciadv.abd1387

Spice, H., Sanloup, C., Cochain, B., de Grouchy, C., and Kono, Y. (2015). Viscosity of liquid fayalite up to 9 GPa. *Geochimica Cosmochimica Acta* 148, 219–227. doi:10.1016/j.gca.2014.09.022

Spiekermann, G., Steele-MacInnis, M., Kowalski, P. M., Schmidt, C., and Jahn, S. (2013). Vibrational properties of silica species in MgO–SiO$_2$ glasses obtained from *ab initio* molecular dynamics. *Chem. Geol.* 346, 22–33. doi:10.1016/j.chemgeo.2012.08.020

Tonks, W. B., and Melosh, H. J. (1993). Magma ocean formation due to giant impacts. *J. Geophys. Res.* 98, 5319–5333. doi:10.1029/92JE02726

Unterborn, C., Schaefer, L., and Krijt, S. (2020). "The composition of rocky planets," in *Planetary Diversity: Rocky planet processes and their observational signatures*. Editors E. J. Tasker, C. Unterborn, M. Laneuville, Y. Fujii, S. J. Desch, and H. E. Hartnett (Bristol: IOP Publishing), 5-1–5-52.

Virgo, D., Mysen, B. O., Danckwerth, P., and Seifert, F. (1982). *Speciation of Fe^{3+} in 1-atm Na$_2$O-SiO$_2$-Fe-O melts*. Carnegie Institution of Washington Year Book, 349–353.

Virgo, D., Mysen, B. O., and Kushiro, I. (1980). Anionic constitution of 1-atmosphere silicate melts: Implications for the structure of igneous melts. *Science* 208, 1371–1373. doi:10.1126/science.208.4450.1371

Virgo, D., and Mysen, B. O. (1985). The structural state of iron in oxidized vs. reduced glasses at 1 atm: A ^{57}Fe mössbauer study. *Phys. Chem. Miner.* 12, 65–76. doi:10.1007/BF01046829

Wacheul, J.-B., Le Bars, M., Monteux, J., and Aurnou, J. M. (2014). Laboratory experiments on the breakup of liquid metal diapirs. *Earth Planet. Sci. Lett.* 403, 236–245. doi:10.1016/j.epsl.2014.06.044

Wang, Y., Sakamaki, T., Skinner, L. B., Jing, Z., Yu, T., Kono, Y., et al. (2014). Atomistic insight into viscosity and density of silicate melts under pressure. *Nat. Commun.* 5, 3241. doi:10.1038/ncomms4241

Waychunas, G. A., Apted, M. J., and Brown, G. E., Jr (1983). X-Ray K-edge absorption spectra of Fe minerals and model compounds: Near-edge structure. *Phys. Chem. Minerals* 10 (1), 1–9. doi:10.1007/bf01204319

Wilke, M., Farges, F., Petit, P. E., Brown, G. E., Jr, and Martin, F. (2001). Oxidation state and coordination of Fe in minerals: An Fe K-XANES spectroscopic study. *American Mineralogist* 86 (5–6), 714–730. doi:10.2138/am-2001-5-612

Wilke, M., Farges, F., Partzsch, G., Thunder, M., Schmidt, C., and Behrens, H. (2007). Speciation of Fe in silicate glasses and melts by *in-situ* XANES spectroscopy. *Am. Mineralogist* 92, 44–56. doi:10.2138/am.2007.1976

Wilke, M., Partzsch, G. M., Bernhardt, R., and Lattard, D. (2004). Determination of the iron oxidation state in basaltic glasses using XANES at the K-edge. *Chem. Geol.* 213, 71–87. doi:10.1016/j.chemgeo.2004.08.034

Xie, L., Yoneda, A., Katsura, T., Andrault, D., Tange, Y., and Higo, Y. (2021). Direct viscosity measurement of peridotite melt to lower-mantle conditions: A further support for a fractional magma-ocean solidification at the top of the lower mantle. *Geophys. Res. Lett.* 48, e2021GL094507. doi:10.1029/2021GL094507

You, J.-L., Jiang, G.-C., Hou, H.-Y., Chen, H., Wu, Y.-Q., and Xu, K.-D. (2005). Quantum chemistry study on superstructure and Raman spectra of binary sodium silicates. *J. Raman Spectrosc.* 36, 237–249. doi:10.1002/jrs.1287

Zakaznova-Herzog, V. P., Malfait, W. J., Herzog, F., and Halter, W. E. (2007). Quantitative Raman spectroscopy: Principles and application to potassium silicate glasses. *J. Non-Crystalline Solids* 353, 4015–4028. doi:10.1016/j.jnoncrysol.2007.06.033

Zhang, H. L., Cottrell, E., Solheid, P. A., Kelley, K. A., and Hirschmann, M. M. (2018). Determination of Fe^{3+}/ΣFe of XANES basaltic glass standards by Mössbauer spectroscopy and its application to the oxidation state of iron in MORB. *Chem. Geol.* 479, 166–175. doi:10.1016/j.chemgeo.2018.01.006

Zhang, H. L., Hirschmann, M. M., Cottrell, E., and Withers, A. C. (2017). Effect of pressure on Fe^{3+}/ΣFe ratio in a mafic magma and consequences for magma ocean redox gradients. *Geochimica Cosmochimica Acta* 204, 83–103. doi:10.1016/j.gca.2017.01.023

Zotov, N., Ebbsjö, I., Timpel, D., and Keppler, H. (1999). Calculation of Raman spectra and vibrational properties of silicate glasses: Comparison between Na$_2$Si$_4$O$_9$ and SiO$_2$ glasses. *Phys. Rev. B* 60, 6383–6397. doi:10.1103/physrevb.60.6383